

A statistical study towards high-mass BGPS clumps with the MALT90 survey

Xiao-Lan Liu^{1,2}, Jin-Long Xu^{1,2}, Chang-Chun Ning³, Chuan-Peng Zhang^{1,2} and Xiao-Tao Liu⁴

¹ National Astronomical Observatories, Chinese Academy of Sciences, Beijing 100012, China;
liuxiaolan@bao.ac.cn

² NAOC-TU Joint Center for Astrophysics, Lhasa 850000, China

³ Tibet University, Lhasa 850000, China

⁴ Department of Finance, Central China Normal University, Wuhan 430079, China

Received 2017 June 7; accepted 2017 September 24

Abstract In this work, we perform a statistical investigation towards 50 high-mass clumps using data from the Bolocam Galactic Plane Survey (BGPS) and Millimetre Astronomy Legacy Team 90-GHz survey (MALT90). Eleven dense molecular lines ($\text{N}_2\text{H}^+(1-0)$, $\text{HNC}(1-0)$, $\text{HCO}^+(1-0)$, $\text{HCN}(1-0)$, $\text{HN}^{13}\text{C}(1-0)$, $\text{H}^{13}\text{CO}^+(1-0)$, $\text{C}_2\text{H}(1-0)$, $\text{HC}_3\text{N}(10-9)$, $\text{SiO}(2-1)$, $^{13}\text{CS}(2-1)$ and $\text{HNCO}(4_{4,0} - 3_{0,3})$) are detected. N_2H^+ and HNC are shown to be good tracers for clumps in various evolutionary stages since they are detected in all the fields. The detection rates of N-bearing molecules decrease as the clumps evolve, but those of O-bearing species increase with evolution. Furthermore, the abundance ratios $[\text{N}_2\text{H}^+]/[\text{HCO}^+]$ and $\log([\text{HC}_3\text{N}]/[\text{HCO}^+])$ decline with $\log([\text{HCO}^+])$ as two linear functions, respectively. This suggests that N_2H^+ and HC_3N transform to HCO^+ as the clumps evolve. We also find that C_2H is the most abundant molecule with an order of magnitude 10^{-8} . In addition, three new infall candidates, G010.214–00.324, G011.121–00.128 and G012.215–00.118(a), are discovered to have large-scale infall motions and infall rates with an order of magnitude $10^{-3} M_\odot \text{yr}^{-1}$.

Key words: stars: formation — ISM: abundance — ISM: molecules — radio lines: ISM — ISM: kinematics and dynamics

1 INTRODUCTION

The fate of an individual star is determined by its mass and chemical composition at birth. A massive star has several ways to march towards death, based on its initial mass. Therefore, understanding the initial physical and chemical characteristics of massive stars can promote investigations on stellar structure and evolution. However, it is difficult to be sure of the exact initial properties of these stars just through observations and numerical simulations. We had better establish a viable theory on star formation to infer the mass and chemistry when the star was born. From decades of research, the theory regarding low-mass star formation is relatively mature and relies on disc accretion and driven molecular outflows

(Shu et al. 1987). However, various formation scenarios for high-mass stars are widely debated in the literature (e.g. Zinnecker & Yorke 2007; Beuther et al. 2007; Tan et al. 2014). Core accretion (McKee & Tan 2002, 2003) and competitive accretion (Bonnell et al. 2001, 2004) are two controversial theories underlying current studies (He et al. 2016). The core accretion model, similar to low-mass star formation, essentially presumes that the star's environment has no great impact on the evolution of an isolated core. The final mass of a massive star is dominated by self-gravitation, which is assumed to be supported either by thermal pressure, turbulence or magnetic fields (McKee & Tan 2002, 2003). This model emphasizes a direct link between the core and the star, and therefore the core mass function (CMF) will have a sim-

ilar shape to the stellar initial mass function (IMF) (e.g. Motte et al. 1998). However for the competitive accretion model, the circumstellar environment plays a vital role in the mass of a star, since a set of cores with different masses competitively accrete materials from their surrounding envelopes. Most of the higher-mass cores fragment into sub-cores and the majority of these sub-cores do not continue to accrete significantly such that their masses are set from the fragmentation process. In addition, a few higher-mass cores continue to accrete and become higher-mass stars (Bonnell & Bate 2006). Hence, the competitive accretion model can explain the full range and distribution of stellar masses (Bonnell et al. 2001).

From the perspective of observations, the later competitive accretion scenario seems more suitable for massive star formation since cases of an individual massive star accompanying numerous low-mass stars around a cluster have been frequently detected (Bressert et al. 2012). Each of these observations just represents a kind of evolutionary state at a moment, not a continuous forming process. Instead, a statistical study towards a sample consisting of high-mass cores in different evolutionary stages can help us to deduce the various laws describing the physical and chemical features during the evolution of high-mass star formation. Adopting Spitzer 3.6, 4.5, 8.0 and 24 μm images, Guzmán et al. (2015) classified all Millimetre Astronomy Legacy Team 90-GHz (MALT90) survey clumps by visual inspection into four consecutive evolutionary stages: quiescent (pre-stellar), proto-stellar, HII region and photodissociation region (PDR). In terms of the mid-infrared characteristics, quiescent clumps seem dark at 3.6–24 μm . Proto-stellar clumps either contain a 24 μm point source or are associated with an “extended green object” (EGO; Cyganowski et al. 2008). The unresolved 24 μm emission, mostly produced by relatively hot dust (≥ 40 K) (Faimali et al. 2012; Zhang et al. 2016), indicates the existence of embedded stars or protostars, whereas an EGO results from shocks generated by molecular outflows. Both HII regions and PDRs show extended 8 μm emission, which originates mainly from polycyclic aromatic hydrocarbons (PAHs; Watson et al. 2008) at 8 μm bandpass.

In this paper, we carry out a statistical study towards 50 high-mass clumps using 1.1 mm continuum data from the Bolocam Galactic Plane Survey (BGPS), together with molecular lines from MALT90, aiming at exploring the environment where the massive stars form.

Given that the dust emission is optically thin in molecular clouds, the 1.1 mm data can be utilized to display the internal structures and derive physical information within clumps such as the H_2 column densities, dust temperatures, masses and volume densities. Alternatively, the optically thin spectra $\text{N}_2\text{H}^+(1-0)$, $\text{HN}^{13}\text{C}(1-0)$ and $\text{H}^{13}\text{CO}^+(1-0)$ can trace the internal structures of clumps and fragmentation of clumps, and provide velocity information for the observed sources, an important factor for deriving distances. The optically thick lines $\text{HNC}(1-0)$ and $\text{HCO}^+(1-0)$ are good indicators of infall motions, implying the existence of star formation. Furthermore, we also research the chemical compositions, properties and evolutions by analyzing the molecular lines. With regard to the remaining parts of this paper, Section 2 gives a description about the data archive and Section 3 is about the results. A discussion is presented in Section 4. We summarize our conclusions in Section 5.

2 DATA AND SAMPLE

2.1 Archival Data

BGPS¹ (Glenn et al. 2009) is a 1.1 mm continuum survey of the Galactic plane made using Bolocam (Glenn et al. 2003; Haig et al. 2004) on the Caltech Submillimeter Observatory (CSO). This mm band traces thermal dust emission, which can reveal repositories of dense molecular gases, ranging in scale from cores to entire clouds. Hence, the connection between these gases and star formation regions can be explored. The BGPS has a full width at half-maximum (FWHM) effective beam size of 33'' and in total covers 192 square degrees, including a blind survey of the inner Galaxy spanning the areas $-10^\circ < l < 90.5^\circ$ where $|b| < 0.5^\circ$, the Cygnus X spiral arm ($75.5^\circ \leq l \leq 87.5^\circ$, $|b| \leq 1.5^\circ$), cross-cuts ($l = 3^\circ, 15^\circ, 30^\circ, 31^\circ$, $|b| \leq 1.5^\circ$), and four targeted regions in the outer Galaxy which are IC 1396 (9 square degrees, $97.5^\circ \leq l \leq 100.5^\circ$, $2.25^\circ \leq b \leq 5.25^\circ$), a region towards the Perseus Arm (4 square degrees centered on $l = 111$, $b = 0$ near NGC7538), W3/4/5 (18 square degrees, $132.5^\circ \leq l \leq 138.5^\circ$), along with Gem OB1 (6 square degrees, $187.5^\circ \leq l \leq 193.5^\circ$). Rosolowsky et al. (2010) compiled a source catalog of this survey, which consists of 8358 sources and is 98% complete from 0.4 Jy to 60 Jy over all object sizes for which the survey is sensitive ($< 3.5'$).

¹ http://irsa.ipac.caltech.edu/data/BOLOCAM_GPS/

The MALT90 Survey (Jackson et al. 2013) is a large international project conducted with the ATNF Mopra 22-m telescope, which simultaneously images 16 molecular lines near 90 GHz with the on-the-fly (OTF) mapping mode. These dense molecular lines characterize the physical and chemical conditions of the high-mass star formation clumps in different evolutionary stages (pre-stellar, proto-stellar, HII and PDR). This survey covers the Galactic longitude ranges $300^\circ < l < 357^\circ$ (4th quadrant) and $3^\circ < l < 20^\circ$ (1st quadrant), with effective angular and spectral resolutions of $\sim 36''$ and $\sim 0.11 \text{ km s}^{-1}$, respectively. The final data were recorded in the antenna temperature scale of T_A^* (K) and the sensitivity ($T_A^* \times \text{rms}$ at 0.11 km s^{-1}) is about 0.2 K. The conversion for line intensities to the main beam brightness temperature scale is made using the formula $T_{\text{MB}} = T_A^*/\eta_{\text{MB}}$, where η_{MB} is the main beam efficiency of about 0.49 at 86 GHz and 0.44 at 110 GHz (Ladd et al. 2005). Extrapolation using the Ruze formula gives η_{MB} values in the range 0.49–0.46 for the 86.75–93.17 GHz frequency range of MALT90. The MALT90 data were obtained from the online archive² and reduced by the software packages Continuum and Line Analysis Single-Dish Software (CLASS) and Grenoble Graphic (GREG)³.

The Spitzer IRAC 8 μm , MIPS 24 μm , Herschel PACS 70 and 160 μm together with SPIRE 250, 350 and 500 μm images were downloaded from the Galactic Legacy Infrared Mid-Plane Survey Extraordinaire (GLIMPSE), a 24 and 70 Micron Survey of the Inner Galactic Disk with MIPS (MIPSGAL)⁴ and the Herschel Science Archive (HSA)⁵ (Poglitsch et al. 2010; Griffin et al. 2010).

2.2 Source Selection and Classification

In order to characterize the high-mass clumps, the sample used in this study is a sub-sample from the BGPS catalog, satisfying the following points: (a) all the sources in the sample are covered in the survey region of MALT90; (b) the equivalent radius of each BGPS clump is at least twice the beam size of MALT90 (about $36''$), for the sake of reducing the beam dilution and distinguishing two cores within the same clump; (c) each BGPS clump in the sample has at least one molecular line detected

whose signal-to-noise ratio is at or above the 3σ limit. As a result, 48 BGPS clumps are chosen first. Then seeing the $\text{N}_2\text{H}^+(1-0)$ emission in Section 3.3, we find that clumps G12.215–00.118 and G354.00+00.474 both contain two distinguishable sub-structures (G12.215–00.118(a) and G12.215–00.118(b), G354.00+00.474(a) and G354.00+00.474(b)). This means 50 clumps are finally identified.

Table 1 presents some basic information for the 50 clumps from the BGPS catalog (ID, clump name, longitude and latitude of the peak, deconvolved angular radius, $40''$ aperture flux density and integrated flux density). However, the peaks of G12.215–00.118(a), G12.215–00.118(b), G354.00+00.474(a) and G354.00+00.474(b) in Table 1 correspond to the peaks of the N_2H^+ emission within them and offset from the previous ones measured by Rosolowsky et al. (2010). In addition, referring to the classification towards all the MALT90 survey clumps of Guzmán et al. (2015), we find that our sample comprises 2 PDRs, 25 HII regions, and 19 proto-stellar, 3 per-stellar and 1 uncertain cases. (G12.215–00.118(a), G12.215–00.118(b), G354.00+00.474(a) and G354.00+00.474(b) are reclassified according to the method of Guzmán et al. (2015) with the Spitzer 3.6, 4.5, 8.0 and 24 μm images. G12.215–00.118(a), G354.00+00.474(a) and G354.00+00.474(b) are HII regions, but G12.215–00.118(b) is in an earlier stage of proto-stellar evolution.) Column (16) of Table 1 lists the evolutionary stages of all clumps in our sample. We can combine the PDR clumps into HII regions as Hoq et al. (2013) did yielding only two PDR clumps. In short, the selected sample encompasses three different evolutionary stages from pre-stellar (3), proto-stellar (19) to HII/PDR (27).

3 RESULTS

3.1 Detected Species, Distances and Dust Temperatures

Table 2 shows the detected molecular lines of MALT90 and their detection rates. We find 11 spectra are detected. $\text{N}_2\text{H}^+(1-0)$ and $\text{HNC}(1-0)$ are observed towards all the fields. This suggests that these two species are good indicators for tracing the whole procedure of high-mass star formation. The $\text{N}_2\text{H}^+(1-0)$ lines can be used to infer information about velocity and internal structure since they are likely to be optically thin in the molecular clouds. Additionally, the detection rates of $\text{HCO}^+(1-0)$,

² <http://atoa.atnf.csiro.au/MALT90>

³ <http://www.iram.fr/IRAMFR/GILDAS>

⁴ <http://irsa.ipac.caltech.edu/data/SPITZER/GLIMPSE>

⁵ <http://irsa.ipac.caltech.edu/applications/Herschel>

Table 1 The Basic and Derived Clump Parameters

ID	BGPS clumps ^a	<i>l</i>	<i>b</i>	Distance	<i>T_d</i>	<i>R</i>	<i>S₄₀</i>	<i>S_{int}</i>	<i>N_{H2}</i>	<i>n_{H2}</i>	<i>M_{iso}</i>	<i>M_{vir}</i>	Classifi.		
(1)	(2)	(deg)	(deg)	(kpc)	ref	(K)	($''$)	(pc)	(Jy)	(Jy)	(10^{22} cm^{-2})	(10^3 cm^{-3})	(M_{\odot})	(M_{\odot})	(16)
896	G003.254+00.410	3.254	0.41	10.49	3	13.5	66.2	3.4	0.34(0.04)	1.65(0.15)	1.7(0.2)	0.38(0.03)	4207.2(382.5)	5633.2(1691.7)	Quiescent
920	G003.310-00.402	3.310	-0.402	2.93	3	15.5	71.84	1.0	0.85(0.06)	4.22(0.3)	3.5(0.2)	2.21(0.16)	680.8(48.4)	1863.3(210.5)	Protostellar
1129	G005.833-00.511	5.833	-0.511	3.43	1	19.8	71.71	1.2	0.77(0.07)	3.95(0.31)	2.2(0.2)	1.26(0.10)	617.2(48.4)	773.4(122.3)	H II region
1250	G006.919-00.225	6.919	-0.225	2.97	3	13.1	67.93	1.0	0.83(0.07)	4.25(0.32)	4.4(0.4)	3.36(0.25)	910.6(68.6)	1516.5(170.8)	H II region
1290	G007.337-00.015	7.337	-0.015	13.55	3	15.2	65.67	4.3	0.51(0.05)	2.47(0.21)	2.2(0.2)	0.38(0.03)	8772.9(745.9)	3373.3(260.2)	Protostellar
1337	G008.141+00.224	8.142	0.224	2.99	3	26.2	80.81	1.2	2.75(0.19)	14.24(0.95)	5.5(0.4)	2.52(0.17)	1170.3(78.1)	1358.2(134.9)	H II region
1354	G008.352-00.318	8.352	-0.318	4.57	1	27.4	81.4	1.8	0.54(0.07)	2.68(0.29)	1.0(0.1)	0.29(0.03)	486.2(52.6)	1082.2(173.1)	H II region
1412	G009.212-00.202	9.212	-0.202	4.56	1	16.1	64.29	1.4	1.02(0.09)	4.6(0.36)	4.0(0.4)	2.05(0.16)	1700.1(133.0)	1803.5(231.4)	H II region
1416	G009.282-00.148	9.282	-0.148	4.51	1	11.0	72.32	1.6	0.32(0.06)	1.95(0.25)	2.3(0.4)	1.12(0.14)	1282.8(164.5)	1162.7(218.7)	Protostellar
1455	G010.152-00.344	10.152	-0.344	1.26	3	43.0	85.98	0.5	1.92(0.14)	10.33(0.71)	2.1(0.2)	1.98(0.14)	82.8(5.7)	1192.0(152.6)	H II region
1466	*G010.214-00.324	10.214	-0.324	3.12	3	24.3	84.6	1.3	1.56(0.13)	8.3(0.63)	3.5(0.3)	1.35(0.10)	817.8(62.1)	5010.0(631.5)	Protostellar
1467	G010.226-00.208	10.226	-0.208	3.13	3	18.2	98.76	1.5	1.00(0.08)	7.9(0.57)	3.3(0.3)	1.19(0.09)	1154.7(83.3)	2033.4(120.3)	Protostellar
1474	G010.286-00.120	10.286	-0.12	3.55	1	24.0	68.12	1.2	1.71(0.14)	9.41(0.68)	3.9(0.3)	2.62(0.19)	1219.8(88.1)	2251.3(314.8)	H II region
1479	G010.320-00.258	10.32	-0.258	3.05	3	21.4	62.32	0.9	0.86(0.07)	3.36(0.27)	2.3(0.2)	1.65(0.13)	373.8(30.0)	1826.8(167.6)	H II region
1483	G010.343-00.144	10.344	-0.144	3.55	1	25.3	84.87	1.5	1.48(0.13)	8.58(0.61)	3.1(0.3)	1.15(0.08)	1039.2(73.9)	1829.3(100.4)	Protostellar
1507	G010.625-00.338	10.625	-0.338	5.2	1	22.7	86.4	2.2	1.12(0.10)	5.45(0.44)	2.7(0.2)	0.55(0.04)	1630.0(131.6)	3249.6(244.9)	H II region
1528	G010.727-00.332	10.727	-0.332	4.9	2	18.8	66.59	1.6	0.50(0.05)	2.28(0.2)	1.6(0.2)	0.68(0.06)	780.7(68.5)	1036.4(269.8)	Protostellar
1569	G010.999-00.370	10.999	-0.370	16.57	3	16.4	61.06	4.9	0.27(0.04)	1.05(0.13)	1.0(0.2)	0.15(0.02)	4988.5(617.6)	2298.6(497.9)	uncertain
1580	G011.063-00.096	11.063	-0.096	3.38	2	12.2	77.96	1.3	0.34(0.05)	2.63(0.23)	2.0(0.3)	1.36(0.12)	817.9(71.5)	459.7(106.4)	Quiescent
1590	G011.111-00.398	11.111	-0.398	5.2	1	19.9	81.87	2.1	1.19(0.09)	7.43(0.52)	3.4(0.3)	1.04(0.07)	2649.9(185.5)	2989.1(306.6)	H II region
1592*	G011.121-00.128	11.121	-0.128	3.03	3	11.0	68.78	1.0	0.44(0.05)	2.67(0.22)	3.1(0.4)	2.66(0.22)	792.8(65.3)	870.1(143.0)	Protostellar
1684*	G012.215-00.118(a)	12.208	-0.104	14	1	26.85	43.1	2.9	4.21(0.91)	4.21(0.91)	8.2(1.8)	1.02(0.22)	7353.6(1589.5)	13748.3(3030.1)	H II region
1684	G012.215-00.118(b)	12.204	-0.126	14	1	25.1	15.9	1.1	1.88(0.12)	1.88(0.12)	4.0(0.3)	9.84(0.63)	3577.6(228.4)	3155.5(338.1)	Protostellar
1742	G012.627-00.016	12.627	-0.016	13.45	3	18.0	78.87	5.1	1.15(0.09)	5.71(0.41)	3.8(0.3)	0.40(0.03)	15652.1(1123.9)	10082.5(1104.6)	H II region
1747	G012.681-00.182	12.681	-0.182	10.73	3	20.6	86.15	4.5	2.09(0.14)	11.82(0.79)	5.8(0.4)	0.66(0.04)	17127.9(1144.8)	6089.7(839.4)	Protostellar
1758	G012.721-00.216	12.721	-0.216	3.46	1	25.3	65.87	1.1	0.96(0.09)	3.81(0.34)	2.0(0.2)	1.12(0.10)	438.4(39.1)	1876.2(340.2)	H II region
1771	G012.773+00.334	12.773	0.334	2.29	1	23.1	66.76	0.7	1.04(0.09)	5.43(0.43)	2.5(0.2)	2.61(0.21)	307.8(24.4)	216.0(51.4)	H II region
1778	G012.805-00.318	12.805	0.318	1.83	3	18.4	72.81	0.6	0.66(0.07)	3.17(0.3)	2.1(0.2)	2.00(0.19)	156.0(14.8)	421.3(52.9)	H II region
1809	G012.905-00.030	12.905	-0.030	4.6	1	19.4	65.04	1.5	1.03(0.08)	3.56(0.27)	3.1(0.2)	1.17(0.09)	1028.7(78.0)	1471.6(338.1)	H II region
1810	G012.909-00.260	12.909	-0.260	3.06	3	22.4	79.15	1.2	3.17(0.21)	15.85(1.04)	7.8(0.5)	3.57(0.23)	1670.6(109.6)	2258.7(164.2)	H II region
1871	G013.217+00.036	13.217	0.036	4.36	1	20.9	74.1	1.6	0.96(0.09)	6.87(0.51)	2.6(0.2)	1.45(0.11)	1612.0(119.7)	1892.0(158.9)	PDR
1876	G013.245-00.084	13.245	-0.084	3.59	1	12.3	62.1	1.1	0.94(0.08)	3.54(0.29)	5.6(0.5)	3.36(0.27)	1225.6(100.4)	1453.9(185.0)	Protostellar
1883	G013.275-00.336	13.275	-0.336	3.83	1	12.6	83.71	1.6	0.49(0.05)	4.04(0.31)	2.8(0.3)	1.41(0.11)	1531.4(117.5)	943.0(278.9)	Protostellar
2011	G014.194-00.193	14.194	-0.193	3.63	1	15.45	89.07	1.6	1.40(0.11)	8.32(0.6)	5.8(0.5)	1.86(0.13)	2070.1(149.3)	2575.3(109.4)	Protostellar
7528	G349.798+00.108	349.798	0.108	10.72	3	20.9	73.21	3.8	0.50(0.06)	2.87(0.26)	1.4(0.2)	0.26(0.02)	4071.1(368.8)	5078.3(972.2)	Protostellar
7549	G350.177+00.014	350.177	0.014	10.38	3	18.0	81.73	4.1	0.96(0.08)	5.72(0.43)	3.2(0.3)	0.46(0.03)	9338.6(702.0)	10890.6(1136.0)	H II region
7571	G350.521-00.350	350.522	-0.35	3.56	1	19.2	61.21	1.1	0.62(0.07)	2.65(0.26)	1.9(0.2)	1.36(0.13)	465.2(45.6)	1095.2(108.3)	Protostellar
7628	G351.555+00.206	351.556	0.206	11.80	3	29.1	73.84	4.2	2.49(0.18)	11.05(0.8)	4.4(0.3)	0.57(0.04)	12398.9(897.7)	25448.7(7049.6)	H II region
7714	G352.584-00.184	352.584	-0.184	5.1	2	23.2	71.9	1.8	0.85(0.10)	4.94(0.44)	2.0(0.2)	0.85(0.08)	1381.2(123.0)	2080.7(161.4)	PDR
7731	G352.970+00.358	352.97	0.358	1.09	2	18.35	66.07	0.3	0.41(0.09)	2.72(0.33)	1.3(0.3)	3.87(0.47)	47.7(5.8)	1273.2(437.9)	Quiescent
7748	G353.091+00.446	353.092	0.446	0.73	2	19.7	60	0.2	0.79(0.13)	4.35(0.44)	2.3(0.4)	11.19(1.13)	31.0(3.1)	136.1(16.1)	H II region
7749	G353.117+00.366	353.118	0.366	0.74	1	22.8	83.84	0.3	0.86(0.11)	5.82(0.54)	2.1(0.3)	4.45(0.41)	35.0(3.3)	128.4(24.0)	Protostellar
7758	G353.316-00.256	353.316	-0.256	3.11	1	14.2	85.96	1.3	0.66(0.11)	4.63(0.49)	3.1(0.5)	1.52(0.16)	959.9(101.6)	1545.9(619.9)	Protostellar
7771	G353.412-00.360	353.412	-0.36	3.8	1	22.5	70.35	1.3	11.16(0.7)	47.62(3.01)	27.4(1.7)	12.22(0.77)	7694.8(486.4)	3212.2(157.4)	H II region
7794	G353.978+00.260	353.978	0.26	19.76	3	12.0	97.81	9.4	0.52(0.08)	5.03(0.48)	3.2(0.5)	0.23(0.02)	54925.5(5241.4)	6917.9(1475.5)	Protostellar
7806	G354.208-00.036	354.208	-0.036	11.69	3	26.3	62.71	3.6	0.73(0.10)	2.75(0.32)	1.5(0.2)	0.26(0.03)	3437.9(400.0)	6514.8(814.3)	H II region
7832	G354.600+00.474(a)	354.6	0.470	4.2	1	24.8	38.26	0.8	3.58(0.54)	3.58(0.54)	7.7(1.2)	4.55(0.69)	622.7(93.9)	1091.8(92.4)	H II region
7832	G354.600+00.474(b)	354.617	0.470	4.2	1	24.1	25.06	0.5	3.89(0.59)	3.89(0.59)	8.7(1.3)	18.27(2.77)	702.0(106.5)	792.4(115.4)	H II region
7836	G354.662+00.484	354.662	0.484	12.59	1	24.2	63.53	3.9	1.09(0.16)	5.26(0.58)	2.4(0.4)	0.50(0.06)	8484.3(935.5)	2678.9(263.6)	H II region
7874	G355.268-00.270	355.268	-0.27	1.29	1	14.7	61.07	0.4	1.06(0.10)	4.19(0.39)	4.7(0.4)	8.80(0.82)	141.8(13.2)	849.0(67.5)	Protostellar

Notes: ^a Sources are named by Galactic coordinates of BGPS sources. An * indicates an infall candidate. References for distance: (1) He et al. (2015), (2) He et al. (2016), (3) this paper. The columns are as follows: (1) clump ID; (2) clump name; (3)–(4) coordinates of the peak; (5) distance; (6) references for the distances; (7) dust temperature; (8)–(9) the effective physical radius in units of arcsecond and pc, respectively; (10) $40''$ aperture flux density; (11) integrated flux density; (12) column density; (13) volume density; (14) clump mass derived from the integrated 1.1 mm emission; (15) viral mass and (16) Spitzer classification.

Table 2 Detection Rates of All the Detected Species Along with Their Corresponding Detection Rates in Each Evolutionary Stage

Detected species (1)	Total detection rate (2)	Detection rates in each evolutionary stage		
		(3)	(4)	(5)
N ₂ H ⁺ (1–0)	100%(50)	100%(3)	100%(19)	100%(27)
HNC(1–0)	100%(50)	100%(3)	100%(19)	100%(27)
HCO ⁺ (1–0)	98.0%(49)	100%(3)	100%(19)	96.3%(26)
HCN(1–0)	86.0%(43)	100%(3)	94.7%(18)	85.2%(23)
HN ¹³ C(1–0)	30.0%(15)	0(0)	36.8%(7)	29.7%(8)
H ¹³ CO ⁺ (1–0)	52.0%(26)	33.3%(1)	47.4%(9)	59.3%(16)
C ₂ H(1–0)	66.0%(33)	0(0)	63.2%(12)	77.8%(21)
HC ₃ N(10–9)	46.0%(23)	33.3%(1)	42.1%(8)	51.9%(14)
SiO(2–1)	10.0%(5)	33.3%(1)	0.05%(1)	11.1%(3)
HNCO(4 _{4,0} – 3 _{0,3})	0.02%(1)	33.3%(1)	0(0)	0(0)
¹³ CS(2–1)	0.02%(1)	0(0)	0(0)	0.04%(1)
		pre-stellar	proto-stellar	HII/PDR

Notes: Quantities in parentheses represent the detected numbers that are represented as a percentage.

HCN(1–0) and HN¹³C(1–0) eventually decline with the evolutionary stages, but those of H¹³CO⁺(1–0), C₂H(1–0) and HC₃N(10–9) present upward tendencies. This implies that nitrogen-bearing, oxygen-bearing and carbon-bearing species are evolving. Furthermore, we find five clumps with SiO emission, excited by shocks from the outflows. HNCO(4_{4,0} – 3_{0,3}) is usually used to trace the hot core and shock-chemistry. In this work it is detected only in the pre-stellar clump G003.254+00.410, which is close to the Galactic center. Only clump G353.412–00.360 exhibits ¹³CS(2–1) emission.

Distances of 30 clumps have been obtained from the literature. For the remaining 20 sources, combining the radial velocities of N₂H⁺(1–0) (see Table 3, Column (6)), we can derive their distances using the Bayesian Distance Calculator⁶ (Reid et al. 2016), which leverages the results to significantly improve the accuracy and reliability of distance estimates to other sources known to follow a spiral structure. This calculator has been proved to be more reliable by Paron et al. (2013) through a comparison with the well-known distances of several HII regions and one supernova remnant, which are close to the results calculated from the Bayesian Distance Calculator. Therefore, it is utilized in this work. The derived distances for the 50 clumps are listed in Column (5) in Table 1.

Moreover, Figure 1 shows the systemic velocity (V_{LSR} of N₂H⁺(1–0) from Sect. 3.4) and the distance distributions of 50 clumps along Galactic longitude. Obviously, the sources in our sample are concentrated

around two active star formation regions: the molecular ring (1st quadrant) and the expanding arm (4th quadrant).

On the other hand, the dust temperatures of the objects in our sample are taken from Guzmán et al. (2015), except for G12.215–00.118(a), G12.215–00.118(b), G354.600+00.474(a) and G354.600+00.474(b), because they deviate from the original peaks of BGPS G12.215–00.118 and G354.600+00.474. We derive their temperatures by ourselves based on the pixel-by-pixel spectral energy distribution (SED) method provided by Wang et al. (2015). The high-quality Hi-GAL data covering a wide spread in wavelength (70–500 μm) can be utilized to investigate the dust properties of entire clouds. Following the steps of Wang et al. (2015), first we should remove the background. A Fourier transform (FT) can transfer the original images into Fourier domain and separate low and high spatial frequency components. The low-frequency component represents large-scale background and foreground emission, while the high-frequency component maintains the emission of interest. Then an inverse FT returns them into the image domain. Detailed illustrations of this FT method can be found in Wang et al. (2015). After removing the background and foreground emission, we convolve the images to the same resolution of 45'' and rebin them to the same pixel size of 11.5'', corresponding to the measured beam and pixel size of Hi-GAL observations at 500 μm (Traficante et al. 2011).

For each pixel, the intensity varies with wavelength as

$$S_\nu = B_\nu(1 - e^{-\tau_\nu}), \quad (1)$$

⁶ <http://bessel.vlbi-astrometry.org/bayesian>

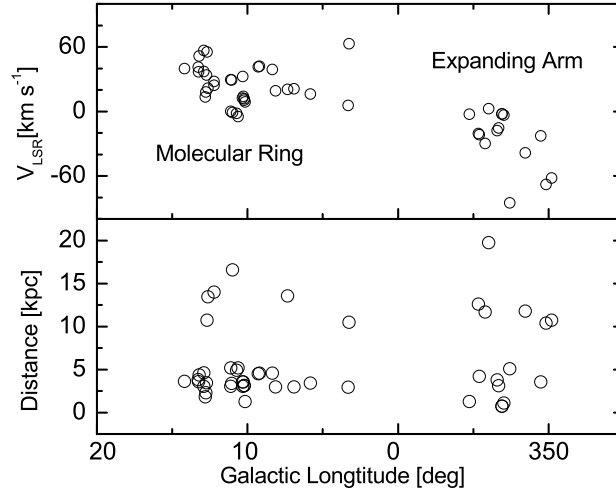


Fig. 1 *Upper panel*: Systemic velocities derived from the Gaussian fittings towards $N_2H^+(1-0)$ lines vs. Galactic longitude distribution towards 50 clumps. *Lower panel*: Distances vs. Galactic longitude distribution towards 50 clumps.

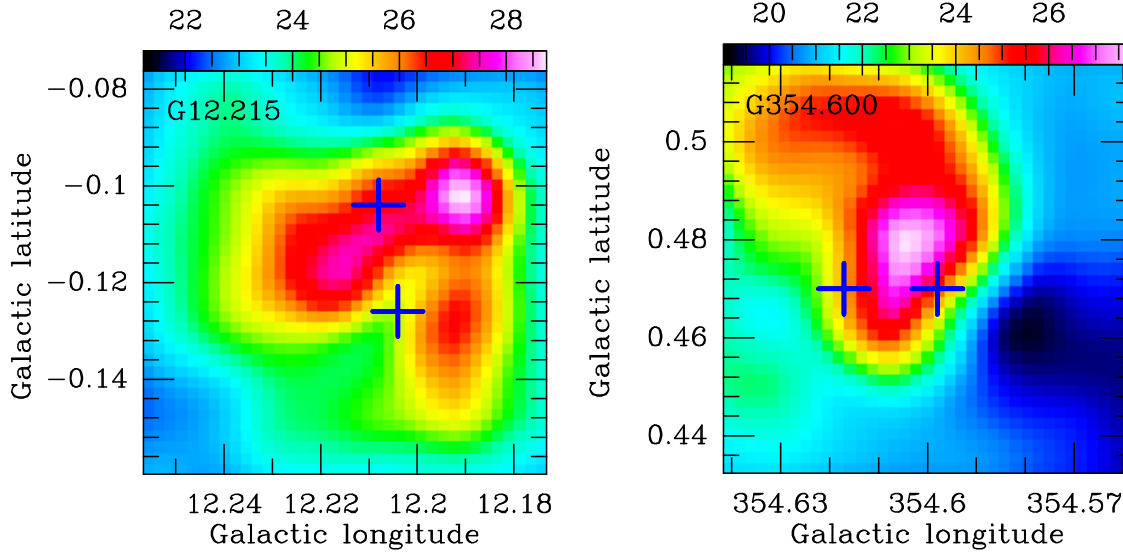


Fig. 2 Maps of the dust temperature T_{dust} towards G12.215-00.118 (*left*) and G354.600+00.474 (*right*) built on the SED fitting pixel by pixel. The “+” symbols in each panel mark the peak positions of the sub-structures.

in which Planck function B_ν is modified by optical depth

$$\tau_\nu = \mu_{H_2} m_H \kappa_\nu N_{H_2} / R_{gd}, \quad (2)$$

where $\mu_{H_2} = 2.8$ is the mean molecular weight considering the contributions of He and other heavy elements to the total mass (Kauffmann et al. 2008). m_H is the mass of a hydrogen atom, N_{H_2} is the column density and $R_{gd} = 100$ is the gas to dust ratio. κ_ν is the dust opacity per gram of gas, expressed as a power law of frequency

(Ossenkopf & Henning 1994)

$$\kappa_\nu = 5.0 \left(\frac{\nu}{600 \text{ GHz}} \right)^\beta \text{ cm}^2 \text{ g}^{-1}, \quad (3)$$

where the dust emissivity index β has been fixed to be 1.75 (Battersby et al. 2011). Therefore, the free parameters are the dust temperature T_{dust} and the H_2 column density N_{H_2} .

Figure 2 shows the temperature distributions towards G12.215-00.118 and G354.600+00.474. The averaged dust temperatures of G12.215-00.118(a),

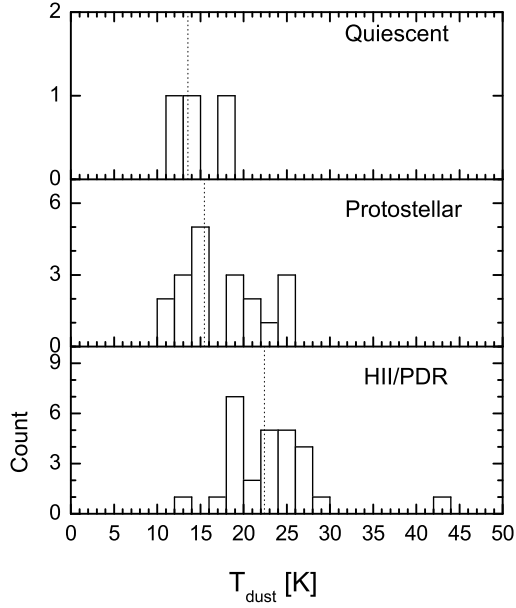


Fig. 3 The dust temperature distributions in each evolutionary stage. The *dashed vertical lines* indicate the median values.

G12.215–00.118(b), G354.600+00.474(a) and G354.600+00.474(b) are 26.9, 25.1, 24.8 and 24.1 K, respectively. All the temperatures are summarized in Column (7) of Table 1.

Figure 3 presents the histogram distributions of T_{dust} . We find the typical ranges of T_{dust} in pre-stellar, proto-stellar and HII/PDR stages to be ~ 10 –12, 14–20 and 18–24 K respectively. The median values are 13.5, 15.5 and 22.5 K respectively. This suggests that the temperatures within the clumps increase as they evolve.

3.2 Clump Masses and Densities

We calculate the beam-averaged H_2 column densities ($N_{\text{H}_2}^{\text{beam}}$) by the following formula

$$N_{\text{H}_2}^{\text{beam}} = \frac{S_\nu(40'')}{\Omega(40'')\mu_{\text{H}_2}m_{\text{H}}\kappa_\nu B_\nu(T_{\text{dust}})R_{\text{gd}}}, \quad (4)$$

where $S_\nu(40'')$ is the flux density in an aperture of diameter $40''$, listed in Column (10) of Table 1. $\Omega(40'') = 2.95 \times 10^{-8}$ sr is the solid angle of the $40''$ aperture. $\kappa_\nu = 0.01114 \text{ cm}^2 \text{ g}^{-1}$ at 271.1 GHz is the dust opacity per gram of gas and dust interpolated from Equation (3). $B_\nu(T_{\text{dust}})$ is the Planck function evaluated at T_{dust} . Meanwhile, we apply an aperture correction of 1.46 to $S_\nu(40'')$ due to sidelobes of the CSO beam (Aguirre et al. 2011). Here, we use $S_\nu(40'')$ as a measure of the flux within a beam since the solid angle of the $40''$ aperture is very close to the solid

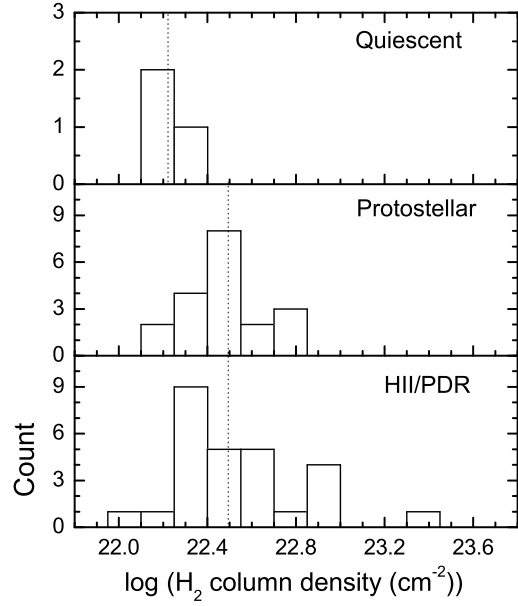


Fig. 4 H_2 column density histograms in each evolutionary stage. The *dashed vertical lines* indicate their median values.

angle of the $33''$ effective beam ($\Omega(33'') = 2.9 \times 10^{-8}$ sr). For G12.215–00.118(a), G12.215–00.118(b), G354.600+00.474(a) and G354.600+00.474(b), we also remeasure their radii and integrated 1.1 mm fluxes.

From Table 1, we find the radii of G12.215–00.118(b), G354.600+00.474(a) and G354.600+00.474(b) are smaller than the $40''$ aperture, while that of G12.215–00.118(a) is around $40''$. Therefore, we substitute their integrated fluxes for $S_\nu(40'')$. $\Omega(40'')$ is still used for them because of beam dilution. Values for the obtained $N_{\text{H}_2}^{\text{beam}}$ are listed in Column (12) of Table 1.

Figure 4 presents histograms of $N_{\text{H}_2}^{\text{beam}}$ in pre-stellar, proto-stellar and HII/PDR stages, from top to bottom respectively. We find that the median values of H_2 column density are $(1.7 \pm 0.2) \times 10^{22}$, $(3.1 \pm 0.2) \times 10^{22}$ and $(3.1 \pm 0.4) \times 10^{22} \text{ cm}^{-2}$ from pre-stellar clumps to HII/PDR. The above result indicates that the peak H_2 column density increases from pre-stellar to proto-stellar and HII/PDR. It suggests that clumps eventually accumulate more materials as they evolve. However, the nearly equal median N_{H_2} from proto-stellar to HII/PDR might be attributed to the eventual strengthened feedbacks in the later evolutionary stage which are likely to disrupt the parent clumps.

The isothermal dust masses, M_{iso} , can be derived by integrated 1.1 mm flux of the whole source via the ex-

pression

$$\begin{aligned}
 M_{\text{iso}} &= \frac{S_\nu D^2}{R_{\text{bg}}} \kappa_\nu B_\nu(T_{\text{dust}}) \\
 &= 13.1 M_\odot \left(\frac{S_\nu}{1 \text{ Jy}} \right) \left(\frac{D}{1 \text{ kpc}} \right)^2 \\
 &\quad \times \left(\frac{e^{13.0 \text{ K}/T_{\text{dust}}} - 1}{e^{13.0 \text{ K}/20.0 \text{ K}} - 1} \right),
 \end{aligned} \quad (5)$$

where S_ν is the integrated 1.1 mm flux. D is the distance. We plot histograms of M_{iso} in various evolutionary stages in Figure 5. The median value per evolutionary stage (from pre-stellar, proto-stellar to HII/PDR respectively) is 818 ± 72 , 1155 ± 83 and $1220 \pm 88 M_\odot$, increasing slightly as a function of the evolutionary stage. This supports the possibility that clumps accumulate material continuously and efficiently with their evolution. In addition, the mass distributions of clumps in different stages are eventually concentrated at $\sim 10^3 M_\odot$ as they evolve.

Furthermore, we calculate the effective radius R and the average H_2 volume density \bar{n} according to the below relations

$$R \simeq D\Theta, \quad (6)$$

$$\bar{n} = 3M_{\text{iso}} / (4\pi R^3 \mu_{\text{H}_2} m_{\text{H}}), \quad (7)$$

where Θ is the effective angular radius, and M_{iso} is the clump mass as calculated in Equation (5). The final results of R and \bar{n} are summarized in Columns (9) and (13) of Table 1 respectively.

Figure 6 shows the effective radii and the average H_2 volume density distributions.

From Figure 6, we find that the median radius from proto-stellar sources (1.5 pc) to HII/PDR clumps (1.3 pc) presents an inward contraction tendency, while the average H_2 volume density shows an increase with evolution. The median \bar{n} values from pre-stellar to proto-stellar to HII/PDR clumps are $(1.36 \pm 0.12) \times 10^3$, $(1.41 \pm 0.11) \times 10^3$ and $(1.45 \pm 0.11) \times 10^3 \text{ cm}^{-3}$, respectively. Both characteristics seem to support the evolutionary tendency that the clumps will become denser and more compact.

3.3 Spatial Distributions of the Spectral-line Emission

In Table 2, 11 out of 16 molecular lines of MALT90 and $\text{N}_2\text{H}^+(1-0)$ are detected in all 50 clumps. So first, we employ this line to determine the velocity information (the centroid velocity and the integrated velocity interval) and the internal structure associated with each

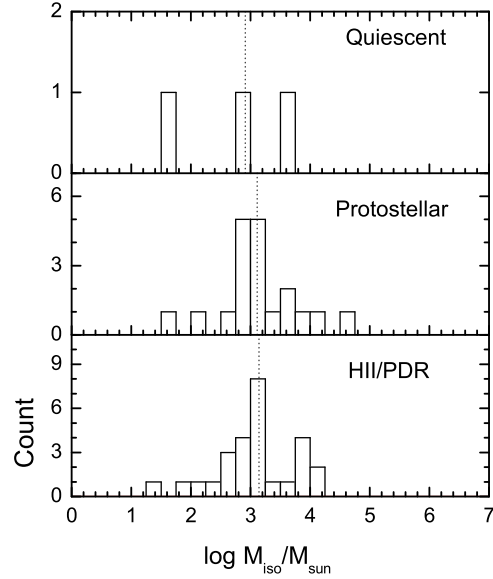


Fig. 5 The clump mass distributions in each evolutionary stage. The *dashed vertical lines* indicate their median values.

clump. The match between the $\text{N}_2\text{H}^+(1-0)$ emission and the 1.1 mm continuum image for every clump provides us with the integrated velocity range of each clump, as shown in Table 3. Based on these velocity ranges, we make integrated intensity maps of the detected spectral lines towards the clumps in this subsection. We did not use the 0th moment maps or the integrated intensity maps included in the MALT90 data archive, since the integrated velocity interval of each clump did not exactly match the clump. We remade the 0th moment maps and improved their corresponding uncertainties. The typical 1σ errors were found to be $\sim 0.5 - 2 \text{ K km s}^{-1}$ for the detected lines.

The remade 0th moment maps are presented in Figure 7, where the magenta contours indicating the molecular emission are overlaid on the BGPS 1.1 mm continuum data. The blue “+” symbols mark the peaks listed in Columns (2) and (3) of Table 1. The contour levels begin at a value of at least 3σ , in order to get rid of the artificial signal and for illustrative purposes.

Figure 7 only shows the detected line emission, associated with the BGPS 1.1 mm continuum emission. These figures demonstrate that all the clumps are a single-core structure, except G12.215–00.118 and G354.600+00.474. They exhibit a two-core structure. This can be explained by the nearly equal effective beam sizes between BGPS 1.1 mm data ($33''$) and the MALT90 survey ($36''$) or the possibility that the spatial resolution of the telescope is not enough. So, we need higher

Table 3 The Derived Line Parameters of the Observed Sources. Quantities in Parentheses Give the Uncertainties

BGPS clumps	Range (km s ⁻¹)	Lines	T_{mb} (K)	$\int T_{\text{mb}} dV$ (K km s ⁻¹)	V_{LSR} (km s ⁻¹)	ΔV (km s ⁻¹)
(1)	(2)	(3)	(4)	(5)	(6)	(7)
G003.254+00.410	(48.06–79.00)	N ₂ H ⁺ (1–0)	1.61(0.28)	35.29(1.02)	63.0(0.37)	11.1(1.67)
		HNC(1–0)	1.85(0.27)	34.62(0.99)	62.69(0.30)	18.69(0.73)
		HCO ⁺ (1–0)	0.91(0.28)	20.85(1.02)	50.68(1.08)	53.90(2.57)
		HCN(1–0)	1.97(0.29)	56.01(1.06)	55.6(0.47)	34.2(1.80)
		SiO(2–1)	0.96(0.28)	23.37(1.02)	62.52(0.80)	28.30(2.01)
		HC ₃ N(10–9)	1.06(0.27)	14.14(0.99)	62.58(0.41)	12.25(1.13)
		HNCO(4 _{4,0} –3 _{0,3})	0.71(0.22)	9.36(0.80)	62.16(0.73)	13.67(2.07)
G003.310–00.402	(2.45–9.28)	N ₂ H ⁺ (1–0)	1.91(0.43)	8.74(0.72)	5.59(0.12)	3.46(0.20)
		HNC(1–0)	1.63(0.31)	6.32(0.52)	5.81(0.22)	3.72(0.56)
		HCO ⁺ (1–0)	1.33(0.30)	5.01(0.50)	5.55(0.20)	3.50(0.50)
		HCN(1–0)	0.90(0.31)	3.41(0.52)	5.44(0.45)	3.50(0.93)
G003.254+00.410	(48.06–79.00)	N ₂ H ⁺ (1–0)	1.61(0.28)	35.29(1.02)	63.0(0.37)	11.1(1.67)
		HNC(1–0)	1.85(0.27)	34.62(0.99)	62.69(0.30)	18.69(0.73)
		HCO ⁺ (1–0)	0.91(0.28)	20.85(1.02)	50.68(1.08)	53.90(2.57)
		HCN(1–0)	1.97(0.29)	56.01(1.06)	55.6(0.47)	34.2(1.80)
		SiO(2–1)	0.96(0.28)	23.37(1.02)	62.52(0.80)	28.30(2.01)
		HC ₃ N(10–9)	1.06(0.27)	14.14(0.99)	62.58(0.41)	12.25(1.13)
		HNCO(4 _{4,0} –3 _{0,3})	0.71(0.22)	9.36(0.80)	62.16(0.73)	13.67(2.07)
G003.310–00.402	(2.45–9.28)	N ₂ H ⁺ (1–0)	1.91(0.43)	8.74(0.72)	5.59(0.12)	3.46(0.20)
		HNC(1–0)	1.63(0.31)	6.32(0.52)	5.81(0.22)	3.72(0.56)
		HCO ⁺ (1–0)	1.33(0.30)	5.01(0.50)	5.55(0.20)	3.50(0.50)
		HCN(1–0)	0.90(0.31)	3.41(0.52)	5.44(0.45)	3.50(0.93)
G005.833–00.511	(14.2–18.64)	N ₂ H ⁺ (1–0)	3.33(0.36)	7.98(0.49)	16.3(0.06)	1.97(0.17)
		HNC(1–0)	2.52(0.33)	7.55(0.45)	15.97(0.11)	3.19(0.26)
		HCO ⁺ (1–0)	4.50(0.32)	14.29(0.44)	15.94(0.06)	3.41(0.14)
		HCN(1–0)	1.80(0.34)	6.35(0.47)	16.3(0.21)	3.46(0.33)
		HN ¹³ C(1–0)	0.95(0.28)	2.73(0.38)	16.15(0.24)	2.68(0.45)
		C ₂ H(1–0)	1.24(0.33)	3.15(0.45)	16.45(0.20)	2.53(0.37)
		H ¹³ CO ⁺ (1–0)	2.28(0.41)	6.42(0.56)	16.77(0.15)	2.89(0.37)
G006.919–00.225	(18.86–24.51)\(26.63–30.10) ^a	N ₂ H ⁺ (1–0)	2.71(0.23)	11.39(0.36)	21.1(0.06)	3.12(0.18)
		HNC(1–0)	2.70(0.28)	8.53(0.44)	21.78(0.18)	4.23(0.55)
		HCO ⁺ (1–0)	2.59(0.27)	5.86(0.42)	23.23(0.08)	2.30(0.22)
		HCN(1–0)	1.29(0.25)	2.57(0.31)	27.9(0.08)	1.51(0.21)
		HN ¹³ C(1–0)	0.81(0.26)	1.86(0.32)	21.42(0.23)	2.22(0.53)
		H ¹³ CO ⁺ (1–0)	0.66(0.22)	2.05(0.27)	21.44(0.31)	3.09(0.56)
		HC ₃ N(10–9)	1.03(0.22)	2.54(0.27)	21.27(0.15)	2.22(0.43)
G007.337–00.015	(17.11–22.13)	N ₂ H ⁺ (1–0)	3.43(0.19)	9.53(0.27)	20.5(0.03)	2.21(0.09)
		HNC(1–0)	2.17(0.21)	7.13(0.30)	19.97(0.08)	3.44(0.21)
		HCO ⁺ (1–0)	1.02(0.19)	4.01(0.27)	20.42(0.23)	5.91(0.56)
		HCN(1–0)	0.86(0.20)	2.86(0.29)	19.6(0.17)	3.03(0.39)
		HN ¹³ C(1–0)	0.74(0.23)	1.58(0.33)	20.51(0.21)	1.82(0.49)
		H ¹³ CO ⁺ (1–0)	0.90(0.18)	2.03(0.26)	20.82(0.21)	2.01(0.56)
		HC ₃ N(10–9)	0.64(0.13)	1.80(0.19)	20.05(0.25)	2.64(0.58)
G008.141+00.224	(15.94–22.27)	N ₂ H ⁺ (1–0)	3.50(0.31)	11.50(0.50)	19.2(0.06)	2.64(0.14)
		HNC(1–0)	3.14(0.25)	10.14(0.41)	19.50(0.07)	3.01(0.17)
		HCO ⁺ (1–0)	2.94(0.35)	9.66(0.57)	20.18(0.10)	3.06(0.27)
		HCN(1–0)	1.92(0.30)	3.81(0.49)	19.9(0.11)	1.92(0.27)
		HN ¹³ C(1–0)	0.80(0.15)	2.11(0.24)	18.16(0.26)	2.59(0.50)
		C ₂ H(1–0)	1.03(0.27)	4.46(0.44)	18.87(0.27)	4.73(0.75)
		H ¹³ CO ⁺ (1–0)	1.12(0.33)	2.13(0.54)	19.33(0.20)	1.99(0.42)
G008.352–00.318	(35.94–41.99)	HC ₃ N(10–9)	0.94(0.28)	3.46(0.45)	19.20(0.29)	3.52(0.73)
		N ₂ H ⁺ (1–0)	2.57(0.27)	6.51(0.42)	39.0(0.06)	1.86(0.17)
		HNC(1–0)	2.55(0.24)	8.63(0.38)	39.14(0.08)	3.13(0.19)
		HCO ⁺ (1–0)	4.10(0.23)	14.99(0.36)	38.88(0.05)	3.69(0.14)
		HCN(1–0)	3.33(0.30)	11.30(0.47)	39.1(0.06)	2.89(0.12)
		C ₂ H(1–0)	1.21(0.24)	3.39(0.38)	38.87(0.16)	2.74(0.39)

Table 3 — Continued.

BGPS clumps	Range (km s ⁻¹)	Lines	T_{mb} (K)	$\int T_{\text{mb}} dV$ (K km s ⁻¹)	V_{LSR} (km s ⁻¹)	ΔV (km s ⁻¹)
(1)	(2)	(3)	(4)	(5)	(6)	(7)
G009.212–00.202	(38.86–45.96)	H ¹³ CO ⁺ (1–0)	0.72(0.13)	1.56(0.20)	39.43(0.25)	1.98(0.54)
		HC ₃ N(10–9)	0.74(0.25)	1.95(0.39)	38.71(0.31)	2.24(0.77)
		N ₂ H ⁺ (1–0)	2.79(0.23)	10.86(0.40)	42.1(0.06)	2.86(0.19)
		HNC(1–0)	3.24(0.20)	6.58(0.35)	42.29(0.08)	3.63(0.35)
		HCO ⁺ (1–0)	2.94(0.19)	9.14(0.33)	42.46(0.09)	5.22(0.39)
		HCN(1–0)	0.81(0.23)	4.06(0.40)	41.53(0.39)	7.65(1.02)
		HN ¹³ C(1–0)	1.17(0.25)	3.62(0.43)	42.53(0.17)	2.77(0.49)
		C ₂ H(1–0)	0.73(0.21)	2.72(0.36)	42.90(0.25)	3.54(0.60)
G009.282–00.148	(37.96–43.84)	H ¹³ CO ⁺ (1–0)	0.71(0.22)	2.87(0.38)	41.68(0.33)	3.76(0.93)
		HC ₃ N(10–9)	0.75(0.21)	1.62(0.36)	42.35(0.20)	2.16(0.40)
		N ₂ H ⁺ (1–0)	2.13(0.24)	7.30(0.38)	41.4(0.06)	2.14(0.21)
		HNC(1–0)	2.51(0.23)	5.07(0.36)	41.22(0.12)	2.87(0.20)
		HCO ⁺ (1–0)	2.79(0.23)	7.18(0.36)	41.00(0.10)	3.71(0.22)
		HCN(1–0)	1.47(0.25)	3.24(0.39)	40.6(0.18)	2.84(0.32)
		H ¹³ CO ⁺ (1–0)	0.94(0.21)	1.59(0.33)	41.99(0.16)	2.23(0.52)
		N ₂ H ⁺ (1–0)	1.98(0.31)	12.76(0.64)	8.76(0.14)	3.86(0.26)
G010.152–00.344	(4.56–14.88)	HNC(1–0)	2.37(0.30)	15.04(0.62)	9.07(0.15)	6.19(0.34)
		HCO ⁺ (1–0)	2.56(0.34)	12.56(0.71)	7.69(0.15)	5.20(0.34)
		HCN(1–0)	1.12(0.32)	2.94(0.67)	8.10(0.26)	1.84(0.54)
		C ₂ H(1–0)	1.67(0.24)	8.78(0.50)	9.31(0.16)	5.04(0.36)
		H ¹³ CO ⁺ (1–0)	0.99(0.23)	4.24(0.48)	10.06(0.22)	4.08(0.48)
		HC ₃ N(10–9)	0.85(0.24)	3.14(0.50)	9.45(0.26)	3.74(0.51)
		N ₂ H ⁺ (1–0)	3.24(0.37)	14.26(0.56)	10.6(0.15)	4.99(0.32)
		HNC(1–0)	2.25(0.36)	9.60(0.54)	8.74(0.18)	5.43(0.64)
*G010.214–00.324	(6.7–12.13)\(-3.0–5.81) ^a	HCO ⁺ (1–0)	2.40(0.36)	7.85(0.54)	7.64(0.16)	4.67(0.48)
		HCN(1–0)	0.86(0.24)	2.06(0.47)	1.68(0.90)	6.03(1.51)
		C ₂ H(1–0)	0.95(0.30)	4.16(0.45)	11.04(0.45)	7.20(1.13)
		HC ₃ N(10–9)	1.18(0.29)	3.87(0.44)	11.16(0.24)	4.61(0.50)
		N ₂ H ⁺ (1–0)	4.93(0.27)	18.50(0.52)	11.9(0.04)	2.93(0.09)
		HNC(1–0)	1.82(0.23)	9.11(0.45)	11.91(0.13)	5.03(0.28)
		HCO ⁺ (1–0)	1.49(0.25)	7.49(0.48)	12.39(0.18)	4.84(0.40)
		HCN(1–0)	0.97(0.30)	5.03(0.58)	10.5(0.28)	2.32(0.52)
G010.226–00.208	(7.19–16.0)	HN ¹³ C(1–0)	0.63(0.13)	1.38(0.25)	11.63(0.29)	2.69(0.58)
		C ₂ H(1–0)	0.76(0.25)	1.90(0.48)	11.45(0.45)	2.43(0.44)
		H ¹³ CO ⁺ (1–0)	0.88(0.23)	2.42(0.45)	12.08(0.20)	2.62(0.39)
		N ₂ H ⁺ (1–0)	5.89(0.61)	23.19(0.95)	14.0(0.09)	3.45(0.25)
		HNC(1–0)	2.74(0.58)	10.36(0.91)	13.23(0.20)	3.94(0.45)
		HCO ⁺ (1–0)	2.91(0.60)	13.63(0.94)	13.07(0.24)	6.04(0.64)
		HCN(1–0)	1.89(0.58)	8.02(0.91)	12.7(0.48)	4.25(0.69)
		N ₂ H ⁺ (1–0)	1.91(0.22)	7.32(0.34)	32.5(0.11)	3.60(0.17)
G010.286–00.120	(10.58–16.51)	HNC(1–0)	1.29(0.24)	5.19(0.38)	31.63(0.18)	4.36(0.42)
		HCO ⁺ (1–0)	1.00(0.26)	2.37(0.41)	32.87(0.17)	1.55(0.50)
		N ₂ H ⁺ (1–0)	4.78(0.25)	16.47(0.41)	12.3(0.03)	2.75(0.08)
G010.320–00.258	(29.15–35.03)	HNC(1–0)	3.06(0.24)	12.87(0.39)	12.59(0.08)	4.50(0.21)
		HCO ⁺ (1–0)	4.59(0.24)	17.44(0.39)	12.87(0.05)	3.87(0.13)
		HCN(1–0)	1.51(0.25)	7.14(0.41)	11.9(0.21)	3.59(0.37)
G010.343–00.144	(9.45–15.54)	HN ¹³ C(1–0)	0.84(0.25)	2.43(0.41)	12.41(0.25)	2.61(0.73)
		C ₂ H(1–0)	1.73(0.26)	4.85(0.42)	12.18(0.13)	2.48(0.50)
		H ¹³ CO ⁺ (1–0)	0.83(0.23)	2.11(0.37)	12.29(0.21)	2.28(0.50)
		HC ₃ N(10–9)	1.35(0.22)	5.13(0.36)	12.22(0.15)	4.03(0.40)
		N ₂ H ⁺ (1–0)	3.13(0.25)	11.63(0.41)	–4.79(0.06)	3.05(0.12)
		HNC(1–0)	2.49(0.23)	10.72(0.37)	–4.27(0.09)	4.49(0.20)
		HCO ⁺ (1–0)	3.10(0.22)	14.53(0.36)	–4.33(0.08)	5.25(0.17)
		HCN(1–0)	2.34(0.24)	10.63(0.39)	–4.98(0.15)	4.15(0.18)
G010.625–00.338	(–7.24 ~ –1.16)	C ₂ H(1–0)	0.86(0.22)	3.32(0.36)	–4.35(0.25)	3.95(0.58)
		HC ₃ N(10–9)	0.82(0.22)	1.50(0.36)	–4.70(0.18)	1.78(0.44)

Table 3 — Continued.

BGPS clumps	Range (km s^{-1})	Lines	T_{mb} (K)	$\int T_{\text{mb}} dV$ (K km s^{-1})	V_{LSR} (km s^{-1})	ΔV (km s^{-1})
(1)	(2)	(3)	(4)	(5)	(6)	(7)
G010.727–00.332	(–3.53–1.42)	$\text{N}_2\text{H}^+(1-0)$	2.31(0.29)	4.36(0.42)	–1.71(0.08)	1.98(0.28)
		$\text{HNC}(1-0)$	2.71(0.23)	7.09(0.33)	–1.48(0.07)	2.92(0.15)
		$\text{HCO}^+(1-0)$	4.63(0.29)	11.00(0.42)	–1.58(0.05)	2.65(0.11)
		$\text{HCN}(1-0)$	2.56(0.27)	5.90(0.39)	–1.15(0.14)	2.80(0.23)
		$\text{C}_2\text{H}(1-0)$	0.95(0.25)	1.61(0.36)	–1.43(0.22)	3.02(0.39)
G010.999–00.370	(–2.63–1.29)	$\text{N}_2\text{H}^+(1-0)$	1.55(0.19)	3.58(0.25)	–0.94(0.07)	1.67(0.20)
		$\text{HNC}(1-0)$	0.75(0.18)	2.27(0.23)	–0.65(0.21)	3.46(0.44)
		$\text{HCO}^+(1-0)$	0.69(0.19)	2.26(0.25)	–0.90(0.27)	4.27(0.58)
G011.063–00.096	(27.63–31.67)	$\text{N}_2\text{H}^+(1-0)$	1.56(0.22)	3.83(0.29)	29.2(0.06)	1.59(0.20)
		$\text{HNC}(1-0)$	1.71(0.24)	4.63(0.31)	29.06(0.11)	2.86(0.28)
		$\text{HCO}^+(1-0)$	0.74(0.17)	1.99(0.22)	28.36(0.30)	3.92(0.71)
		$\text{HCN}(1-0)$	0.63(0.20)	1.11(0.26)	28.9(0.23)	1.79(0.38)
G011.111–00.398	(–1.61–2.62)	$\text{N}_2\text{H}^+(1-0)$	3.60(0.28)	10.95(0.36)	0.16(0.08)	3.00(0.16)
		$\text{HNC}(1-0)$	2.11(0.29)	4.91(0.38)	–1.17(0.14)	3.61(0.39)
		$\text{HCO}^+(1-0)$	1.98(0.32)	3.41(0.42)	–1.79(0.14)	3.54(0.34)
		$\text{HCN}(1-0)$	0.92(0.21)	2.02(0.27)	–1.21(0.29)	3.45(0.64)
		$\text{C}_2\text{H}(1-0)$	0.92(0.31)	2.83(0.40)	0.14(0.30)	3.72(0.68)
		$\text{H}^{13}\text{CO}^+(1-0)$	1.17(0.26)	2.27(0.34)	–0.73(0.15)	1.96(0.42)
		$\text{HC}_3\text{N}(10-9)$	0.94(0.17)	1.80(0.22)	–0.30(0.24)	3.22(0.50)
		$\text{N}_2\text{H}^+(1-0)$	2.21(0.30)	6.58(0.45)	29.6(0.09)	2.35(0.20)
*G011.121–00.128	(26.88–32.17)	$\text{HNC}(1-0)$	1.68(0.26)	4.46(0.39)	28.58(0.16)	2.89(0.40)
		$\text{HCO}^+(1-0)$	0.96(0.23)	5.06(0.76)	26.85(0.34)	4.94(0.96)
		$\text{HCN}(1-0)$	1.02(0.29)	3.15(0.44)	28.7(0.23)	2.93(0.39)
		$\text{HN}^{13}\text{C}(1-0)$	1.05(0.21)	3.18(0.32)	30.13(0.27)	2.68(0.57)
		$\text{C}_2\text{H}(1-0)$	0.74(0.18)	2.26(0.27)	30.59(0.36)	3.38(0.77)
		$\text{N}_2\text{H}^+(1-0)$	1.73(0.29)	15.92(0.68)	24.3(0.40)	5.54(0.62)
		$\text{HNC}(1-0)$	1.93(0.31)	10.34(0.72)	23.31(0.20)	6.62(0.31)
		$\text{HCO}^+(1-0)$	2.62(0.36)	13.40(0.84)	22.94(0.18)	4.78(0.48)
*G012.215–00.118(a)	(21.38–34.09)	$\text{HCN}(1-0)$	0.79(0.26)	3.88(0.61)	23.0(0.48)	3.47(0.91)
		$\text{SiO}(2-1)$	0.76(0.23)	4.41(0.54)	23.05(0.36)	3.32(0.95)
		$\text{C}_2\text{H}(1-0)$	0.81(0.30)	3.69(0.70)	24.53(0.44)	5.07(0.89)
		$\text{H}^{13}\text{CO}^+(1-0)$	0.63(0.21)	1.70(0.49)	24.60(0.35)	3.21(0.74)
		$\text{HC}_3\text{N}(10-9)$	0.82(0.25)	3.65(0.58)	24.05(0.52)	6.78(1.06)
		$\text{N}_2\text{H}^+(1-0)$	2.77(0.20)	14.30(0.47)	28.0(0.09)	3.25(0.18)
		$\text{HNC}(1-0)$	2.68(0.21)	14.48(0.49)	27.87(0.08)	4.99(0.21)
		$\text{HCO}^+(1-0)$	3.52(0.24)	20.73(0.56)	27.46(0.08)	5.61(0.18)
G012.215–00.118(b)	(21.38–34.09)	$\text{HCN}(1-0)$	1.67(0.24)	10.04(0.56)	27.3(0.41)	5.75(0.59)
		$\text{C}_2\text{H}(1-0)$	0.72(0.23)	2.29(0.54)	28.04(0.32)	3.28(0.55)
		$\text{N}_2\text{H}^+(1-0)$	2.21(0.30)	12.15(0.57)	21.7(0.11)	3.56(0.20)
		$\text{HNC}(1-0)$	2.44(0.35)	9.71(0.66)	22.11(0.16)	4.74(0.49)
G012.627–00.016	(18.37–27.03)\(16.31–21.09) ^a	$\text{HCO}^+(1-0)$	1.79(0.29)	6.31(0.55)	21.95(0.39)	8.56(1.38)
		$\text{HCN}(1-0)$	0.92(0.27)	3.31(0.39)	18.3(0.24)	2.72(0.57)
		$\text{SiO}(2-1)$	0.65(0.22)	2.39(0.42)	21.29(0.41)	3.94(0.90)
		$\text{HN}^{13}\text{C}(1-0)$	0.71(0.20)	1.78(0.39)	21.55(0.31)	2.72(0.67)
		$\text{H}^{13}\text{CO}^+(1-0)$	0.85(0.17)	2.11(0.32)	21.08(0.29)	2.20(0.59)
		$\text{HC}_3\text{N}(10-9)$	1.05(0.30)	2.44(0.57)	21.37(0.20)	2.05(0.62)
		$\text{N}_2\text{H}^+(1-0)$	1.91(0.20)	7.22(0.31)	55.5(0.09)	2.92(0.21)
		$\text{HNC}(1-0)$	1.53(0.24)	3.68(0.38)	57.76(0.12)	1.90(0.35)
G012.681–00.182	(56.37–62.09)\(60.35–66.59) ^a	$\text{HCO}^+(1-0)$	1.41(0.25)	4.95(0.39)	58.53(0.16)	3.52(0.42)
		$\text{HCN}(1-0)$	1.02(0.26)	3.43(0.42)	63.2(0.47)	2.79(0.49)
		$\text{C}_2\text{H}(1-0)$	0.98(0.22)	2.67(0.34)	56.29(0.24)	4.69(0.71)
		$\text{HC}_3\text{N}(10-9)$	1.07(0.21)	1.01(0.33)	55.38(0.21)	3.93(0.56)
		$\text{N}_2\text{H}^+(1-0)$	1.31(0.20)	5.30(0.35)	33.8(0.13)	3.28(0.31)
		$\text{HNC}(1-0)$	1.84(0.22)	7.28(0.38)	34.17(0.11)	3.81(0.26)
G012.721–00.216	(31.38–38.33)	$\text{HCO}^+(1-0)$	2.19(0.26)	11.11(0.45)	34.21(0.13)	5.42(0.31)
		$\text{HCN}(1-0)$	1.70(0.24)	8.62(0.42)	34.1(0.17)	4.15(0.33)
		$\text{C}_2\text{H}(1-0)$	0.97(0.27)	2.80(0.47)	33.72(0.25)	4.13(0.74)

Table 3 — Continued.

BGPS clumps	Range (km s ⁻¹)	Lines	T_{mb} (K)	$\int T_{\text{mb}} dV$ (K km s ⁻¹)	V_{LSR} (km s ⁻¹)	ΔV (km s ⁻¹)
(1)	(2)	(3)	(4)	(5)	(6)	(7)
G012.773+00.334	(16.00–20.12)	N ₂ H ⁺ (1 – 0)	1.79(0.26)	3.43(0.34)	18.0(0.08)	1.27(0.19)
		HNC(1 – 0)	1.75(0.29)	4.59(0.38)	18.55(0.14)	2.83(0.42)
		HCO ⁺ (1 – 0)	2.62(0.28)	5.03(0.36)	18.95(0.07)	1.86(0.20)
		HCN(1 – 0)	1.91(0.17)	3.97(0.22)	18.8(0.07)	1.89(0.15)
		C ₂ H(1 – 0)	1.15(0.23)	2.80(0.30)	17.78(0.20)	2.28(0.51)
G012.805–00.318	(11.51–16.42)	N ₂ H ⁺ (1 – 0)	3.04(0.20)	8.56(0.29)	13.6(0.04)	2.07(0.14)
		HNC(1 – 0)	0.65(0.15)	1.69(0.22)	13.39(0.32)	2.86(0.65)
G012.905–00.030	(52.09–60.87)\(58.12–67.43) ^a	N ₂ H ⁺ (1 – 0)	4.03(0.21)	13.46(0.41)	56.7(0.13)	2.47(0.30)
		HNC(1 – 0)	1.73(0.20)	9.29(0.39)	56.91(0.12)	5.44(0.33)
		HCO ⁺ (1 – 0)	2.83(0.23)	7.34(0.45)	58.55(0.06)	2.18(0.17)
		HCN(1 – 0)	0.87(0.22)	5.05(0.44)	62.0(0.72)	5.70(0.92)
		H ¹³ CO ⁺ (1 – 0)	0.96(0.24)	2.12(0.47)	56.86(0.19)	2.31(0.42)
G012.909–00.260	(33.25–40.31)	HC ₃ N(10 – 9)	0.63(0.21)	1.52(0.41)	56.87(0.28)	3.20(0.78)
		N ₂ H ⁺ (1 – 0)	5.64(0.48)	23.11(0.83)	37.2(0.07)	3.46(0.13)
		HNC(1 – 0)	2.34(0.44)	11.57(0.76)	36.99(0.22)	6.12(0.66)
		HCO ⁺ (1 – 0)	1.74(0.54)	6.07(0.94)	35.19(0.35)	3.47(0.84)
		HN ¹³ C(1 – 0)	1.67(0.42)	5.19(0.73)	36.95(0.20)	2.71(0.63)
		C ₂ H(1 – 0)	1.54(0.41)	5.96(0.71)	37.18(0.26)	3.76(0.69)
		H ¹³ CO ⁺ (1 – 0)	1.61(0.37)	3.96(0.64)	37.32(0.18)	2.62(0.54)
G013.217+00.036	(48.31–55.95)	HC ₃ N(10 – 9)	2.04(0.35)	5.41(0.61)	37.21(0.13)	2.52(0.29)
		N ₂ H ⁺ (1 – 0)	3.86(0.23)	14.10(0.41)	51.6(0.04)	2.72(0.12)
		HNC(1 – 0)	2.77(0.25)	9.90(0.45)	51.24(0.08)	3.37(0.18)
		HCO ⁺ (1 – 0)	1.82(0.29)	8.23(0.52)	51.03(0.16)	4.80(0.54)
		HCN(1 – 0)	1.70(0.31)	6.38(0.55)	51.3(0.17)	3.42(0.29)
		C ₂ H(1 – 0)	1.10(0.24)	2.88(0.43)	51.36(0.16)	2.33(0.49)
G013.245–00.084	(32.05–40.21)	H ¹³ CO ⁺ (1 – 0)	1.05(0.26)	1.42(0.46)	51.73(0.17)	1.94(0.30)
		N ₂ H ⁺ (1 – 0)	2.53(0.26)	10.85(0.48)	36.9(0.07)	2.91(0.19)
		HNC(1 – 0)	2.52(0.28)	10.68(0.52)	36.53(0.10)	4.12(0.25)
		HCO ⁺ (1 – 0)	1.74(0.28)	8.63(0.52)	36.24(0.18)	5.16(0.48)
		HCN(1 – 0)	0.95(0.22)	4.36(0.40)	36.2(0.21)	3.31(0.40)
		HN ¹³ C(1 – 0)	0.99(0.30)	3.22(0.55)	36.45(0.25)	3.09(0.58)
		H ¹³ CO ⁺ (1 – 0)	0.96(0.26)	2.12(0.48)	36.58(0.20)	2.27(0.46)
		HC ₃ N(10 – 9)	0.91(0.25)	3.57(0.46)	36.74(0.22)	3.34(0.75)
G013.275–00.336	(36.06–43.82)	N ₂ H ⁺ (1 – 0)	1.43(0.23)	4.50(0.41)	41.2(0.09)	1.91(0.30)
		HNC(1 – 0)	1.31(0.21)	5.88(0.38)	40.43(0.15)	4.25(0.37)
		HCO ⁺ (1 – 0)	1.09(0.27)	5.41(0.48)	40.15(0.30)	5.72(1.02)
		HCN(1 – 0)	0.66(0.22)	3.97(0.39)	40.7(0.38)	4.31(0.79)
		C ₂ H(1 – 0)	0.79(0.22)	2.10(0.39)	40.64(0.17)	1.58(0.50)
		N ₂ H ⁺ (1 – 0)	4.76(0.22)	21.25(0.45)	39.8(0.04)	3.21(0.07)
		HNC(1 – 0)	3.52(0.24)	17.83(0.49)	39.83(0.07)	4.81(0.18)
G014.194–00.193	(34.41–44.15)	HCO ⁺ (1 – 0)	3.38(0.30)	17.31(0.61)	40.34(0.09)	4.91(0.25)
		HCN(1 – 0)	1.46(0.29)	11.42(0.59)	40.3(0.17)	3.84(0.27)
		SiO(2 – 1)	0.78(0.29)	5.05(0.59)	40.59(0.48)	7.23(1.10)
		HN ¹³ C(1 – 0)	1.04(0.23)	3.45(0.47)	39.70(0.17)	2.60(0.43)
		C ₂ H(1 – 0)	0.83(0.25)	3.91(0.51)	39.70(0.31)	4.29(0.78)
		H ¹³ CO ⁺ (1 – 0)	0.81(0.25)	1.82(0.51)	39.50(0.30)	3.81(0.77)
		HC ₃ N(10 – 9)	1.04(0.24)	5.30(0.49)	40.22(0.26)	4.87(0.56)
		N ₂ H ⁺ (1 – 0)	1.25(0.24)	4.72(0.38)	–61.8(0.15)	2.90(0.29)
		HNC(1 – 0)	0.70(0.23)	3.68(0.36)	–61.78(0.39)	6.52(1.15)
		HCO ⁺ (1 – 0)	0.92(0.23)	5.10(0.36)	–61.44(0.36)	9.03(0.79)
G349.798+00.108	(–64.44 ~ –58.41)	N ₂ H ⁺ (1 – 0)	2.17(0.23)	10.42(0.40)	–68.0(0.10)	4.14(0.22)
		HNC(1 – 0)	1.52(0.21)	9.02(0.36)	–68.08(0.18)	7.41(0.43)
		HCO ⁺ (1 – 0)	0.78(0.26)	4.16(0.45)	–65.26(0.5)	11.42(1.03)
		HN ¹³ C(1 – 0)	0.46(0.25)	2.51(0.43)	–67.61(0.67)	6.64(1.52)
		C ₂ H(1 – 0)	0.68(0.21)	3.15(0.36)	–67.02(0.43)	4.63(0.82)
G350.177+00.014	(–71.68 ~ –64.46)	N ₂ H ⁺ (1 – 0)	2.17(0.23)	10.42(0.40)	–68.0(0.10)	4.14(0.22)
		HNC(1 – 0)	1.52(0.21)	9.02(0.36)	–68.08(0.18)	7.41(0.43)
		HCO ⁺ (1 – 0)	0.78(0.26)	4.16(0.45)	–65.26(0.5)	11.42(1.03)
		HN ¹³ C(1 – 0)	0.46(0.25)	2.51(0.43)	–67.61(0.67)	6.64(1.52)
		C ₂ H(1 – 0)	0.68(0.21)	3.15(0.36)	–67.02(0.43)	4.63(0.82)

Table 3 — Continued.

BGPS clumps	Range (km s ⁻¹)	Lines	T_{mb} (K)	$\int T_{\text{mb}} dV$ (K km s ⁻¹)	V_{LSR} (km s ⁻¹)	ΔV (km s ⁻¹)
(1)	(2)	(3)	(4)	(5)	(6)	(7)
G350.521-00.350	(-25.54 ~ -20.81)	N ₂ H ⁺ (1-0)	3.38(0.29)	10.05(0.40)	-22.7(0.06)	2.49(0.13)
		HNC(1-0)	3.06(0.33)	9.12(0.45)	-23.21(0.09)	2.93(0.21)
		HCO ⁺ (1-0)	1.60(0.32)	4.28(0.44)	-23.77(0.16)	2.89(0.53)
		HCN(1-0)	1.09(0.32)	2.61(0.44)	-23.3(0.14)	2.27(0.53)
		HN ¹³ C(1-0)	0.79(0.27)	2.15(0.37)	-22.96(0.26)	2.54(0.57)
		C ₂ H(1-0)	1.00(0.29)	3.16(0.40)	-22.87(0.28)	3.78(0.79)
		H ¹³ CO ⁺ (1-0)	1.64(0.31)	2.75(0.43)	-22.77(0.12)	1.65(0.23)
G351.555+00.206	(-40.94 ~ -32.41)	HC ₃ N(10-9)	0.95(0.27)	2.50(0.40)	-22.49(0.27)	2.86(0.71)
		N ₂ H ⁺ (1-0)	0.83(0.26)	5.92(0.49)	-38.6(0.51)	6.27(0.88)
		HNC(1-0)	2.23(0.23)	13.18(0.43)	-38.01(0.14)	7.18(0.31)
		HCO ⁺ (1-0)	2.96(0.31)	15.89(0.59)	-37.84(0.15)	6.18(0.44)
		HCN(1-0)	1.64(0.31)	11.76(0.59)	-37.2(0.26)	5.50(0.67)
		C ₂ H(1-0)	0.91(0.24)	5.16(0.45)	-38.09(0.40)	7.14(1.11)
		HC ₃ N(10-9)	0.94(0.26)	3.79(0.49)	-38.15(0.25)	3.97(0.59)
G352.584-00.184	(-87.51 ~ -81.72)	N ₂ H ⁺ (1-0)	3.99(0.28)	13.34(0.44)	-85.0(0.05)	2.68(0.11)
		HNC(1-0)	3.56(0.26)	10.79(0.41)	-84.56(0.06)	2.91(0.15)
		HCO ⁺ (1-0)	4.23(0.30)	12.72(0.47)	-84.22(0.06)	2.89(0.16)
		HCN(1-0)	2.64(0.32)	7.36(0.50)	-84.4(0.09)	2.63(0.21)
		C ₂ H(1-0)	0.69(0.25)	3.01(0.39)	-84.80(0.37)	4.65(0.83)
		HC ₃ N(10-9)	1.34(0.34)	2.97(0.53)	-84.90(0.18)	2.29(0.35)
		H ¹³ CO ⁺ (1-0)	1.05(0.36)	1.44(0.52)	-3.14(0.25)	2.17(0.63)
G352.970+00.358	(-6.19 ~ -1.27)	N ₂ H ⁺ (1-0)	1.33(0.31)	2.86(0.45)	-3.39(0.14)	1.46(0.29)
		HNC(1-0)	2.74(0.29)	6.51(0.42)	-3.38(0.07)	2.15(0.18)
		HCO ⁺ (1-0)	4.26(0.34)	9.50(0.49)	-3.65(0.06)	2.51(0.14)
		HCN(1-0)	1.40(0.33)	3.78(0.47)	-3.41(0.15)	2.32(0.30)
		H ¹³ CO ⁺ (1-0)	1.05(0.36)	1.44(0.52)	-3.14(0.25)	2.17(0.63)
		N ₂ H ⁺ (1-0)	3.85(0.31)	9.36(0.45)	-2.19(0.05)	2.03(0.13)
		HNC(1-0)	3.31(0.29)	9.37(0.42)	-2.37(0.07)	2.91(0.17)
G353.091+00.446	(-5.18 ~ -0.33)	HCO ⁺ (1-0)	4.87(0.37)	10.31(0.53)	-2.91(0.05)	2.00(0.12)
		HCN(1-0)	2.82(0.24)	7.42(0.35)	-2.78(0.07)	2.58(0.15)
		C ₂ H(1-0)	0.99(0.27)	3.34(0.39)	-2.02(0.25)	3.74(0.69)
		H ¹³ CO ⁺ (1-0)	1.47(0.30)	2.25(0.43)	-2.20(0.12)	1.40(0.25)
		N ₂ H ⁺ (1-0)	2.81(0.24)	8.72(0.43)	-2.43(0.04)	1.55(0.17)
		HNC(1-0)	6.82(0.23)	10.63(0.41)	-2.19(0.08)	2.69(0.26)
		HCO ⁺ (1-0)	7.07(0.21)	14.61(0.38)	-1.23(0.05)	3.45(0.17)
G353.117+00.366	(-4.67 ~ -3.07)	HCN(1-0)	1.68(0.24)	10.37(0.43)	-1.58(0.17)	4.35(0.38)
		C ₂ H(1-0)	0.94(0.26)	4.40(0.46)	-1.37(0.30)	5.04(0.83)
		H ¹³ CO ⁺ (1-0)	0.84(0.28)	3.05(0.50)	-1.69(0.33)	2.86(0.74)
		HC ₃ N(10-9)	1.05(0.25)	1.49(0.45)	-2.43(0.13)	1.02(0.25)
		N ₂ H ⁺ (1-0)	1.24(0.27)	4.51(0.48)	-15.5(0.21)	2.75(0.57)
		HNC(1-0)	0.97(0.27)	4.05(0.48)	-15.84(0.32)	5.28(0.72)
		HCO ⁺ (1-0)	1.91(0.29)	8.29(0.52)	-14.94(0.15)	4.33(0.36)
G353.316-00.256	(-17.71 ~ -10.25)	HCN(1-0)	1.03(0.26)	3.48(0.46)	-14.7(0.21)	2.72(0.49)
		N ₂ H ⁺ (1-0)	6.67(0.24)	37.92(0.51)	-17.7(0.05)	3.98(0.10)
		HNC(1-0)	8.09(0.27)	30.18(0.57)	-16.90(0.05)	6.00(0.16)
		HCO ⁺ (1-0)	13.31(0.30)	45.70(0.64)	-16.16(0.03)	6.20(0.11)
		HCN(1-0)	7.52(0.34)	22.45(0.72)	-16.48(0.46)	5.69(0.46)
		SiO(2-1)	1.39(0.21)	9.34(0.45)	-16.3(0.22)	8.86(1.40)
		HN ¹³ C(1-0)	1.20(0.25)	7.08(0.53)	-17.28(0.23)	5.53(0.57)
G353.412-00.360	(-22.26 ~ -11.74)	¹³ CS(2-1)	1.14(0.24)	4.60(0.51)	-16.04(0.18)	3.58(0.50)
		C ₂ H(1-0)	2.19(0.27)	15.13(0.57)	-16.67(0.16)	7.14(0.34)
		H ¹³ CO ⁺ (1-0)	1.97(0.25)	9.74(0.53)	-16.95(0.13)	4.75(0.31)
		HC ₃ N(10-9)	3.00(0.28)	14.87(0.59)	-16.74(0.09)	4.60(0.24)
		N ₂ H ⁺ (1-0)	1.95(0.31)	4.20(0.36)	2.69(0.07)	2.15(0.24)
		HNC(1-0)	2.35(0.26)	4.24(0.30)	3.01(0.08)	1.71(0.22)
		HCO ⁺ (1-0)	0.92(0.29)	2.49(0.33)	2.50(0.30)	4.37(0.70)
G353.978+00.260	(1.21 - 4.41)	HCN(1-0)	1.00(0.33)	2.86(0.38)	2.70(0.32)	3.33(0.54)
		C ₂ H(1-0)	1.01(0.29)	1.84(0.33)	2.56(0.19)	1.70(0.50)

Table 3 — *Continued.*

BGPS clumps	Range (km s ⁻¹)	Lines	T_{mb} (K)	$\int T_{\text{mb}} dV$ (K km s ⁻¹)	V_{LSR} (km s ⁻¹)	ΔV (km s ⁻¹)
(1)	(2)	(3)	(4)	(5)	(6)	(7)
G354.208–00.036	(-31.95 ~ -26.75)	N ₂ H ⁺ (1–0)	1.77(0.24)	6.62(0.35)	-29.7(0.12)	3.38(0.22)
		HNC(1–0)	1.65(0.25)	6.07(0.36)	-30.03(0.15)	4.30(0.41)
		HCO ⁺ (1–0)	1.95(0.27)	5.95(0.39)	-30.74(0.13)	3.97(0.35)
		HCN(1–0)	0.94(0.24)	2.84(0.35)	-30.74(0.17)	1.70(0.31)
		C ₂ H(1–0)	1.03(0.24)	2.85(0.35)	-30.43(0.18)	2.60(0.44)
G354.600+00.474(a)	(-24.86 ~ -17.94)	N ₂ H ⁺ (1–0)	3.90(0.29)	14.00(0.49)	-21.5(0.6)	2.92(0.13)
		HNC(1–0)	2.60(0.28)	10.95(0.47)	-21.19(0.10)	4.05(0.23)
		HCO ⁺ (1–0)	2.65(0.26)	13.71(0.44)	-21.40(0.11)	5.80(0.27)
		HCN(1–0)	1.30(0.33)	9.93(0.55)	-22.5(0.21)	4.68(0.53)
		C ₂ H(1–0)	0.95(0.24)	3.73(0.40)	-20.25(0.24)	4.37(0.55)
		H ¹³ CO ⁺ (1–0)	0.80(0.24)	1.55(0.40)	-21.13(0.23)	2.23(0.45)
G354.600+00.474(b)	(-24.86 ~ -17.94)	N ₂ H ⁺ (1–0)	2.41(0.25)	8.09(0.50)	-20.54(0.09)	3.16(0.24)
		HNC(1–0)	2.09(0.24)	10.05(0.63)	-20.90(0.12)	4.52(0.43)
		HCO ⁺ (1–0)	2.78(0.25)	19.23(0.69)	-20.63(0.11)	6.51(0.30)
		HCN(1–0)	1.27(0.24)	3.89(1.38)	-21.75(0.29)	2.86(0.80)
		C ₂ H(1–0)	0.86(0.19)	3.11(0.57)	-20.53(0.32)	3.41(0.78)
		H ¹³ CO ⁺ (1–0)	0.69(0.22)	2.74(0.46)	-19.65(0.34)	3.76(0.67)
G354.662+00.484	(-22.81 ~ -18.16)	N ₂ H ⁺ (1–0)	4.14(0.23)	9.99(0.32)	-20.6(0.04)	2.02(0.11)
		HNC(1–0)	3.53(0.25)	9.50(0.34)	-20.76(0.06)	2.87(0.14)
		HCO ⁺ (1–0)	4.32(0.29)	14.08(0.40)	-20.81(0.06)	3.34(0.16)
		HCN(1–0)	3.63(0.27)	12.29(0.37)	-20.7(0.08)	3.15(0.16)
		C ₂ H(1–0)	0.92(0.31)	2.73(0.43)	-20.33(0.28)	2.93(0.53)
*G355.268–00.270	(-5.39 ~ -0.59)	N ₂ H ⁺ (1–0)	3.05(0.24)	10.89(0.38)	-2.68(0.08)	3.70(0.15)
		HNC(1–0)	2.03(0.24)	7.83(0.38)	-2.69(0.13)	4.63(0.29)
		HCO ⁺ (1–0)	2.17(0.27)	5.42(0.42)	-2.82(0.19)	4.83(0.82)
		HCN(1–0)	1.29(0.27)	3.27(0.42)	-4.56(0.11)	1.24(0.30)
		H ¹³ CO ⁺ (1–0)	0.73(0.23)	2.41(0.36)	-2.77(0.33)	2.89(0.81)

Notes: ^a There are two velocity ranges associated with the clump. The latter is for HCN(1–0) and the former is for the other detected spectra. * indicates an infall candidate.

The columns are as follows: (1) clump name; (2) integrated velocity interval; (3) detected lines in each clump; (4) main bright temperature; (5) integrated intensity; (6) centroid velocity; (7) line width.

spatial resolution data to further investigate fragmentation within the clumps. Additionally, the emissions of N₂H⁺(1–0), HNC(1–0), HCO⁺(1–0) and HCN(1–0) are more extended than other species. As the clumps evolve, the compositions of the dense gases will be richer and more complicated.

3.4 Spectral Lines and Their Physical Parameters

Figure 7 also shows molecular lines extracted from the peak positions of the clumps. In terms of spectral profiles, the hyperfine structures (hfss) of N₂H⁺(1–0), HCN(1–0) and C₂H(1–0) are detected. However, near 90 GHz, N₂H⁺(1–0) should be split into 15 hfss, out of which seven have a different frequency (Pagani et al. 2009; Keto & Rybicki 2010). C₂H(1–0) presents six hfss (Reitblat 1980; Padovani et al. 2009; Spielfiedel et al. 2012). Here, we find that seven components of

N₂H⁺(1–0) have blended into three components with a relative intensity of 1:5:3. Meanwhile, two hfss ($N_{J,F} = 1_{3/2,2} - 0_{1/2,1}$ and $N_{J,F} = 1_{3/2,1} - 0_{1/2,0}$) of C₂H(1–0) are clearly observed in our MALT90 data. We apply Gaussian fittings to all the detected spectra and the fitting parameters are listed in Table 3. The hfs fittings are not done to N₂H⁺(1–0), HCN(1–0) and C₂H(1–0), since more than 70% of the N₂H⁺(1–0) exhibit an optical depth of 0.1 and over half of the later two lines present bad fittings. The physical parameters displayed in Table 3 are for the main components N₂H⁺ ($N_{J,F} = 1_{2,3} - 0_{1,2}$), HCN ($N_{J,F} = 1_{1,0} - 0_{0,1}$) and C₂H ($N_{J,F} = 1_{3/2,2} - 0_{1/2,1}$). The systemic velocity of each clump is marked by the red dashed lines in Figure 7. In order to find other indicators of systemic velocity, we plot the centroid velocity differences between other molecular lines and N₂H⁺(1–0) in Figure 8.

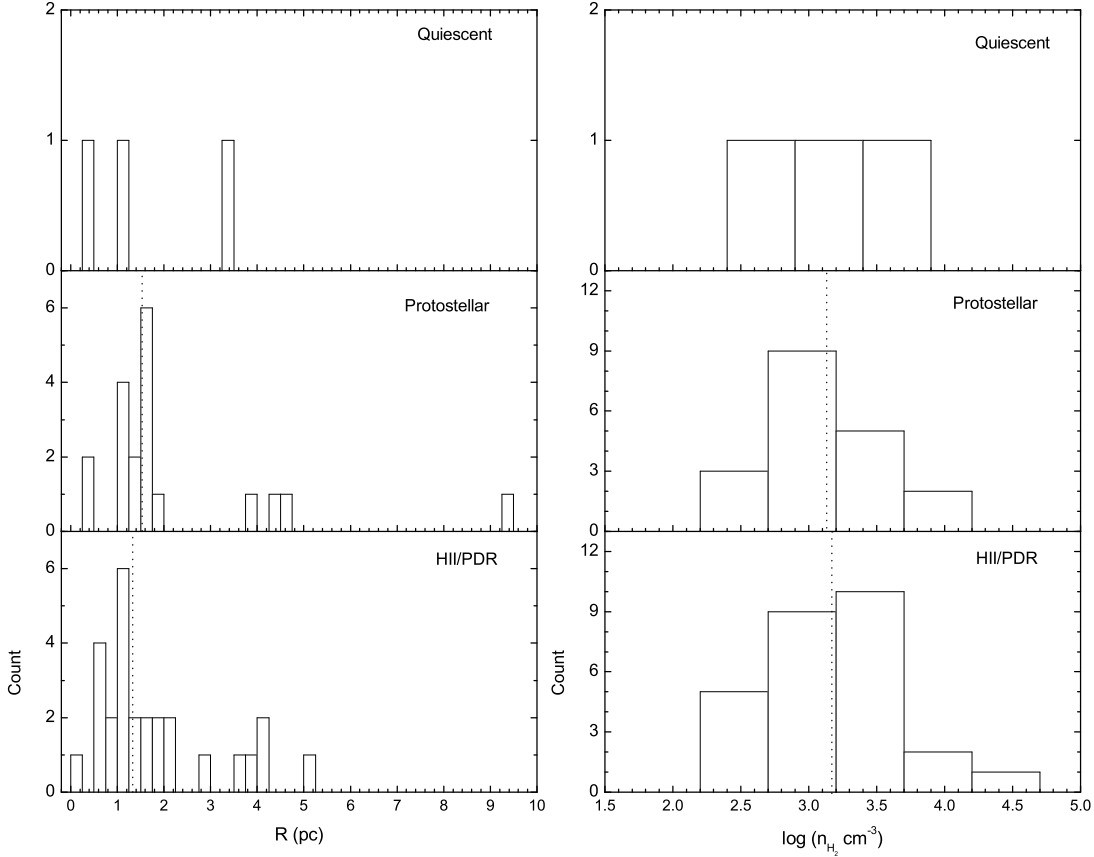


Fig. 6 *Left panel:* histograms of the effective radius R and the average H_2 \bar{n} of clumps in stages from pre-stellar to HII/PDR. The *dashed vertical lines* indicate their median values.

From Figure 8, we realize that the centroid velocities of all the molecular lines appear to coincide with those of $\text{N}_2\text{H}^+(1-0)$, except $\text{HCO}^+(1-0)$ and $\text{HCN}(1-0)$. For $\text{HCO}^+(1-0)$, the V_{LSR} of clump G003.254+00.410 shows an up to 12 km s^{-1} redshift and the remaining clumps present a difference within 3 km s^{-1} . For $\text{HCN}(1-0)$, the V_{LSR} of seven clumps in the 1st quadrant of the Galaxy emerge with large gaps ($3-12 \text{ km s}^{-1}$) compared with those of $\text{N}_2\text{H}^+(1-0)$. The great redshift in clump G003.254+00.410 for $\text{HCO}^+(1-0)$ and $\text{HCN}(1-0)$ can be attributed to the possibility that G003.254+00.410 is located near the Galactic center, where ultraviolet radiation is strong. The centroid velocity differences between $\text{HCO}^+(1-0)$ and $\text{N}_2\text{H}^+(1-0)$ for other clumps may be caused by star formation activities, such as infall motions (see Sect. 4.5). However, the reason why $\text{HCN}(1-0)$ in some clumps greatly shifts (red or blue) from the systemic velocities is still unclear. Perhaps more observations are needed to verify this result.

3.5 Column Densities and Abundances of the Molecules

Under the assumption of local thermodynamic equilibrium (LTE) and a beam filling factor of 1, the column density of molecular lines can be derived from (Sanhueza et al. 2012)

$$N = \frac{3k^2}{16\pi^3\mu^2hB^2R_{\text{in}}} \frac{T_{\text{ex}} + hB/3k}{(J+1)^2} \frac{e^{E_u/kT_{\text{ex}}}}{e^{h\nu/kT_{\text{ex}}} - 1} \times \frac{1}{J(T_{\text{ex}}) - J(T_{\text{bg}})} \frac{\tau}{1 - e^{-\tau}} \int T_{\text{MB}} d\nu, \quad (8)$$

where k is the Boltzmann constant, h is the Planck constant, μ is the permanent dipole moment of the molecule, ν is the transition frequency, J is the rotational quantum number of the lower state, E_u is the energy of the upper level, B is the rotational constant of the molecule, $T_{\text{bg}} = 2.73$ is the background temperature and T_{ex} is the excitation temperature. Here we assume that $T_{\text{ex}} = T_{\text{dust}}$ and $J(T)$ is defined by $J(T) = (e^{h\nu/kT} - 1)^{-1}$. $\int T_{\text{MB}} d\nu$ is the integrated intensity. The values of μ , B and E_u can

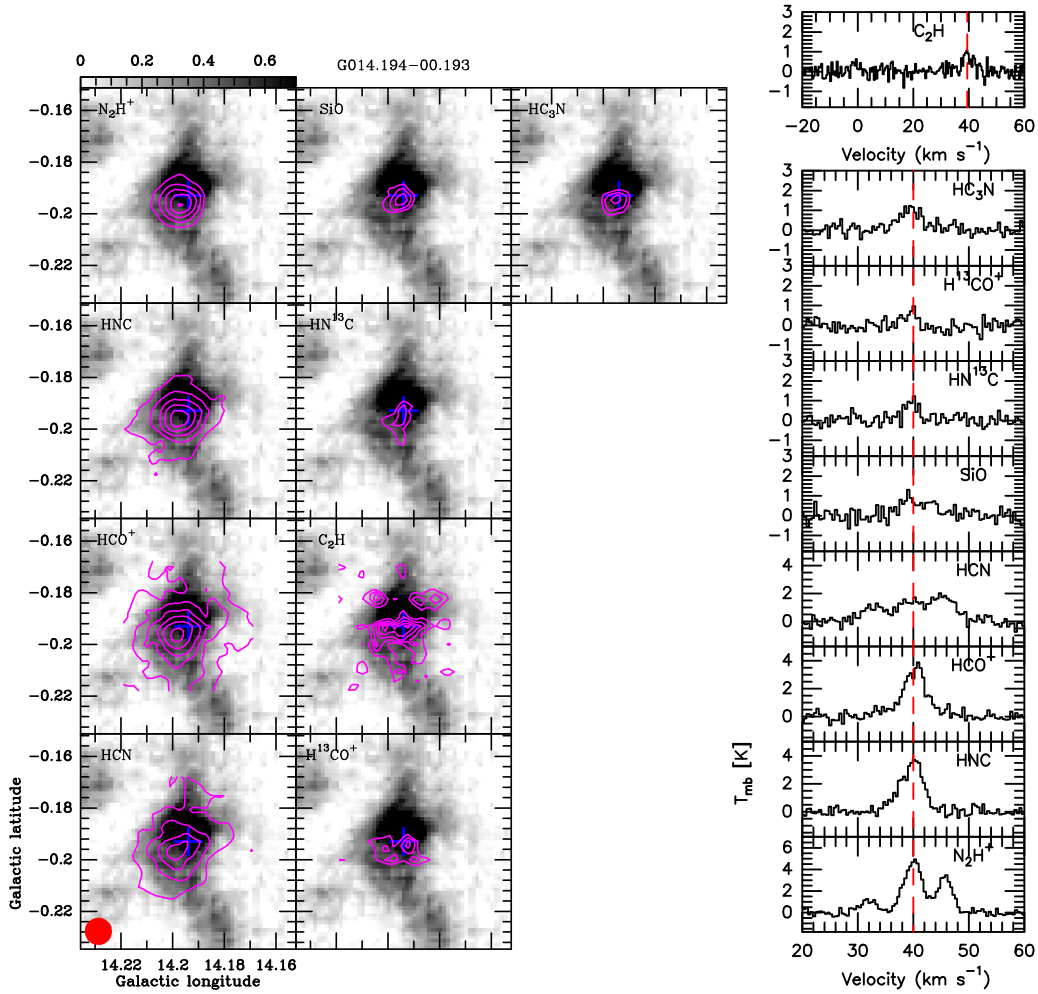


Fig. 7 Example of G014.194–00.193. *Left-panel*: Maps of the BGPS 1.1 mm continuum emission (grey-scale) overlaid with integrated intensity contours of the detected species which are denoted in the *top left* corners. The color bar indicates the flux with units of Jy beam^{-1} for 1.1 mm. The *magenta* contour levels start at 3σ in steps of 0.8σ ($\sigma = 1.29, 1.01, 0.94, 1.03, 0.55, 0.3, 0.33, 0.39, 0.56 \text{ K km s}^{-1}$) in the sequence for subfigures of *top left* to *bottom right* then *top right* to *bottom right*. The symbols “+” mark the peak positions in Table 1. *Right-panel*: The spectra are extracted from the peak position and the *red dashed line* marks the centroid velocity determined by the Gaussian fitting to the $\text{N}_2\text{H}^+(1-0)$ line. The other 47 BGPS clumps are shown at <http://www.raa-journal.org/docs/Supp/ms3409figonline.pdf>.

be obtained from the Cologne Database for Molecular Spectroscopy⁷ (CMDS; Müller et al. 2001, 2005). R_{in} is the relative intensity of the brightest hyperfine transition taking into account the satellite lines corrected by their opacities. It is 5/9 for N_2H^+ , 5/12 for C_2H and fixed to 1.0 for transitions without hfs.

Assuming the same filling factor and excitation temperature, optical depth can be derived from the intensity ratio associated with the spectra of two isotopes, one of which is optically thin.

$$\frac{1 - e^{-r\tau}}{1 - e^{-\tau}} \simeq \frac{T_{\text{MB},1}}{T_{\text{MB},2}}, \quad (9)$$

⁷ <http://www.astro.uni-koeln.de/cmds/>

where r is the intensity ratio of line 1 over line 2, and line 2 is optically thin. $T_{\text{MB},1}$ and $T_{\text{MB},2}$ are the main beam brightness temperatures obtained from the Gaussian fittings. Therefore, both the optical depths of $\text{HN}^{13}\text{C}(1-0)$ and $\text{H}^{13}\text{CO}^+(1-0)$ can be estimated through the isotope abundance ratios of $r \sim [^{12}\text{C}]/[^{13}\text{C}]$. In our work, we assume $[^{12}\text{C}]/[^{13}\text{C}] \simeq 50$ (Purcell et al. 2006). The calculated results of the optical thickness of $\text{HN}^{13}\text{C}(1-0)$ and $\text{H}^{13}\text{CO}^+(1-0)$ are listed in Columns (2) and (3) of Table 4 respectively.

Actually, the molecular lines exhibiting hfs can also be used to derive their optical depths via Equation (9) by applying the intensity ratio of two components (Yu & Xu 2016). For $\text{C}_2\text{H}(1-0)$, two components $N_{J,F} =$

Table 4 The Optical Depths of N_2H^+ , HN^{13}C , H^{13}CO^+ and C_2H , as well as the Column Densities of N_2H^+ , HNC , HCO^+ , C_2H and HC_3N

BGPS clumps	Opacity				Column density				
	N_2H^+	HN^{13}C	H^{13}CO^+	C_2H	N_2H^+ (10^{13} cm^{-2})	HNC (10^{14} cm^{-2})	HCO^+ (10^{14} cm^{-2})	C_2H (10^{14} cm^{-2})	HC_3N (10^{13} cm^{-2})
(1)	(2)	(3)	(4)	(5)	(6)	(7)	(8)	(9)	(10)
HII/PDR									
G005.833–00.511	0.96	0.48	0.71	0.52	4.25(0.27)	1.75(0.24)	3.75(0.33)	4.03(0.58)	...
G006.919–00.225	0.04	0.36	0.29	...	3.13(0.11)	0.70(0.12)	0.38(0.05)	...	1.26(0.13)
G008.141+00.224	0.02	0.29	0.48	1.30	4.86(0.22)	1.00(0.11)	1.03(0.26)	9.77(0.96)	1.37(0.18)
G008.352–00.318	0.05	...	0.20	1.03	2.88(0.18)	...	0.33(0.04)	6.89(0.77)	0.78(0.16)
G009.212–00.202	0.37	0.45	0.27	0.13	3.91(0.14)	1.91(0.23)	0.56(0.07)	2.54(0.34)	0.70(0.16)
G010.152–00.344	5.15	...	0.49	0.55	41.15(2.07)	...	3.13(0.35)	20.90(1.20)	1.43(0.23)
G010.286–00.120	0.51	11.59(0.47)
G010.320–00.258	0.05	2.72(0.13)
G010.625–00.338	0.05	0.37	4.48(0.16)	4.37(0.48)	0.59(0.14)
G011.111–00.398	0.12	...	0.89	2.30	4.00(0.13)	...	1.67(0.25)	7.27(1.03)	0.72(0.09)
G012.215–00.118(a)	0.05	...	0.27	0.98	6.95(0.29)	...	0.47(0.14)	7.22(1.37)	1.45(0.23)
G012.627–00.016	0.05	0.34	0.63	...	4.01(0.18)	0.76(0.17)	1.03(0.16)	...	1.01(0.24)
G012.721–00.216	0.21	0.59	2.39(0.16)	4.42(0.74)	...
G012.773+00.334	0.05	0.39	1.33(0.13)	3.77(0.41)	...
G012.805–00.318	0.20	3.08(0.11)
G012.905–00.030	0.18	...	0.42	...	4.97(0.14)	...	0.72(0.16)	...	0.62(0.17)
G012.909–00.260	0.68	0.99	0.99	0.84	11.88(0.43)	7.48(1.05)	3.52(0.57)	9.60(1.15)	2.14(0.24)
G013.217+00.036	0.62	...	0.87	1.63	6.71(0.20)	...	1.05(0.34)	6.07(0.91)	...
G350.177+00.014	0.87	0.36	...	0.56	5.02(0.20)	1.13(0.19)	...	3.86(0.43)	...
G351.555+00.206	0.05	0.46	2.75(0.23)	8.54(0.74)	1.52(0.20)
G352.584–00.184	0.05	0.37	5.22(0.18)	4.03(0.53)	1.17(0.21)
G353.091+00.446	0.05	...	0.36	2.18	3.28(0.16)	...	0.66(0.13)	8.18(0.96)	...
G353.412–00.360	0.05	0.16	0.16	0.61	14.54(0.20)	1.66(0.12)	1.40(0.08)	22.10(0.84)	5.89(0.23)
G354.208–00.036	0.05	0.41	2.84(0.14)	4.27(0.53)	...
G354.600+00.474(a)	0.08	...	0.36	0.08	5.85(0.20)	...	0.54(0.14)	4.56(0.48)	...
G354.600+00.474(b)	0.04	...	0.29	0.67	1.94(0.20)	...	0.75(0.13)	4.90(0.89)	...
G354.662+00.484	0.06	0.89	4.05 (0.13)	4.75(0.74)	...
median	0.05	0.36	0.39	0.59	4.05 (0.18)	1.40(0.28)	0.89(0.20)	4.90(0.74)	1.22(0.19)
Protostellar									
G003.310–00.402	0.05	2.65(0.22)
G007.337–00.015	0.05	0.42	0.99	...	2.84(0.07)	0.75(0.16)	1.40(0.18)	...	0.81(0.08)
G009.282–00.148	0.24	...	0.42	...	2.05(0.11)	...	0.40(0.08)
G010.214–00.324	0.51	0.86	7.20(0.29)	7.18(0.77)	1.53(0.17)
G010.226–00.208	0.05	0.43	0.89	1.82	6.16(0.18)	0.75(0.14)	1.68(0.31)	3.91(0.98)	...
G010.343–00.144	0.21	0.31	0.20	0.60	7.43(0.18)	1.20(0.20)	0.41(0.07)	7.68(0.67)	2.03(0.14)
G010.727–00.332	0.85	0.90	2.14(0.20)	2.35(0.53)	...
G011.121–00.128	0.05	0.99	...	1.05	1.69(0.11)	3.05(0.31)	...	2.64(0.31)	...
G012.215–00.118(b)	0.05	0.20	5.94(0.20)	3.00(0.36)	...
G012.681–00.182	1.36	1.82	4.64(0.20)	5.95(0.77)	0.40(0.13)
G013.245–00.084	0.05	0.49	0.80	...	2.92(0.13)	1.60(0.27)	1.06(0.24)	...	1.88(0.24)
G013.275–00.336	0.56	0.15	1.55(0.14)	1.73(0.31)	...
G014.194–00.193	0.24	0.36	0.27	0.73	7.02(0.14)	1.42(0.19)	0.35(0.10)	4.70(0.62)	2.35(0.22)
G349.798+00.108	0.05	1.71(0.14)
G350.521–00.350	0.53	0.30	0.99	0.21	4.34(0.18)	0.84(0.15)	2.19(0.34)	3.43(0.43)	1.02(0.16)
G353.117+00.366	0.05	...	0.13	0.97	3.37(0.16)	...	0.36(0.06)	7.58(0.79)	0.59(0.18)
G353.316–00.256	0.05	1.30(0.14)
G353.978+00.260	0.02	0.62	1.10(0.09)	1.85(0.34)	...
G355.268–00.270	0.73	...	0.42	...	4.39(0.16)	...	0.69(0.10)
median	0.05	0.42	0.42	0.80	2.92(0.16)	1.20(0.20)	0.69(0.16)	3.67(0.58)	1.22(0.17)
Quiescent									
G003.254+00.410	0.74	13.66(0.40)	6.86(0.48)
G011.063–00.096	0.05	1.03 (0.07)
G352.970+00.358	0.42	...	0.29	...	1.13 (0.18)	...	0.33(0.12)
Uncertain									
G010.999–00.370	0.05	1.12(0.07)

Table 5 The Abundances of N_2H^+ , HNC, HCO^+ , C_2H and HC_3N

BGPS clumps	N_2H^+ 10^{-9}	HNC 10^{-8}	HCO^+ 10^{-8}	C_2H 10^{-8}	HC_3N 10^{-10}
HII/PDR					
G005.833–00.511	1.93(0.22)	0.80(0.13)	1.70(0.21)	1.85(0.31)	...
G006.919–00.225	0.72(0.07)	0.16(0.03)	0.09(0.01)	...	2.87(0.40)
G008.141+00.224	0.88(0.07)	0.18(0.02)	0.19(0.05)	1.78(0.22)	2.49(0.37)
G008.352–00.318	2.88(0.34)	...	0.33(0.05)	6.89(1.03)	7.76(1.74)
G009.212–00.202	0.97(0.11)	0.48(0.07)	0.14(0.02)	0.62(0.10)	1.76(0.43)
G010.152–00.344	19.60(2.11)	...	1.49(0.22)	9.96(1.10)	6.79(1.26)
G010.286–00.120	2.97(0.25)
G010.320–00.258	1.17(0.13)
G010.625–00.338	1.66(0.13)	1.61(0.22)	2.20(0.55)
G011.111–00.398	1.17(0.11)	...	0.49(0.09)	2.14(0.36)	2.13(0.32)
G012.215–00.118(a)	0.85(0.20)	...	0.06(0.02)	0.89(0.26)	1.77(0.48)
G012.627–00.016	1.06(0.09)	0.20(0.05)	0.27(0.05)	...	2.66(0.66)
G012.721–00.216	1.19(0.14)	2.21(0.43)	...
G012.773+00.334	0.54(0.07)	1.51(0.19)	...
G012.805–00.318	1.48(0.14)
G012.905–00.030	1.60(0.11)	...	0.23(0.05)	...	1.99(0.55)
G012.909–00.260	1.53(0.11)	0.96(0.15)	0.45(0.08)	1.22(0.17)	2.75(0.36)
G013.217+00.036	2.59(0.22)	...	0.41(0.14)	2.33(0.38)	...
G350.177+00.014	1.57(0.16)	0.35(0.07)	...	1.20(0.17)	...
G351.555+00.206	0.63(0.07)	1.94(0.22)	3.46(0.51)
G352.584–00.184	2.61(0.27)	2.02(0.34)	5.87(1.20)
G353.091+00.446	1.42(0.25)	...	0.29(0.07)	3.55(0.74)	...
G353.412–00.360	0.54(0.04)	0.06(0.01)	0.05(0.00)	0.82(0.07)	2.18(0.16)
G354.208–00.036	1.89(0.27)	2.83(0.50)	...
G354.600+00.474(a)	0.76(0.13)	...	0.07(0.02)	0.60(0.12)	...
G354.600+00.474(b)	0.38(0.05)	...	0.09(0.02)	0.58(0.14)	...
G354.662+00.484	1.69(0.29)	1.99(0.46)	...
median	1.42 (0.13)	0.28(0.07)	0.25(0.05)	1.85(0.26)	2.58(0.50)
Protostellar					
G003.310–00.402	0.76(0.07)
G007.337–00.015	1.30(0.13)	0.34(0.08)	0.64(0.10)	...	3.66(0.51)
G009.282–00.148	0.90(0.16)	...	0.17(0.05)
G010.214–00.324	2.05(0.20)	2.04(0.29)	4.37(0.62)
G010.226–00.208	1.87(0.18)	0.23(0.05)	0.51(0.11)	1.18(0.31)	...
G010.343–00.144	2.39(0.23)	0.39(0.08)	0.13(0.03)	2.47(0.31)	6.54(0.78)
G010.727–00.332	1.33(0.22)	1.46(0.38)	...
G011.121–00.128	0.54(0.07)	0.98(0.16)	...	0.86(0.14)	...
G012.215–00.118(b)	1.48(0.13)	0.74(0.10)	...
G012.681–00.182	0.81(0.07)	1.03(0.14)	0.70(0.23)
G013.245–00.084	0.52(0.05)	0.29(0.06)	0.19(0.05)	...	3.35(0.53)
G013.275–00.336	0.56(0.07)	0.62(0.14)	...
G014.194–00.193	1.21(0.11)	0.24(0.04)	0.06(0.02)	0.82(0.12)	4.05(0.51)
G349.798+00.108	1.22(0.20)
G350.521–00.350	2.29(0.25)	0.44(0.09)	1.15(0.22)	1.80(0.29)	5.34(1.02)
G353.117+00.366	1.60(0.25)	...	0.17(0.04)	3.62(0.65)	2.81(0.94)
G353.316–00.256	0.41(0.09)
G353.978+00.260	0.34(0.05)	0.58(0.14)	...
G355.268–00.270	0.94(0.09)	...	0.15(0.03)
median	1.21(0.13)	0.34(0.08)	0.17(0.07)	1.10(0.22)	3.86(0.58)
Quiescent					
G003.254+00.410	8.01(0.92)	40.35(5.52)
G011.063–00.096	0.52(0.09)
G352.970+00.358	0.88(0.25)	...	0.25(0.11)
Uncertain					
G010.999–00.370	1.12(0.23)

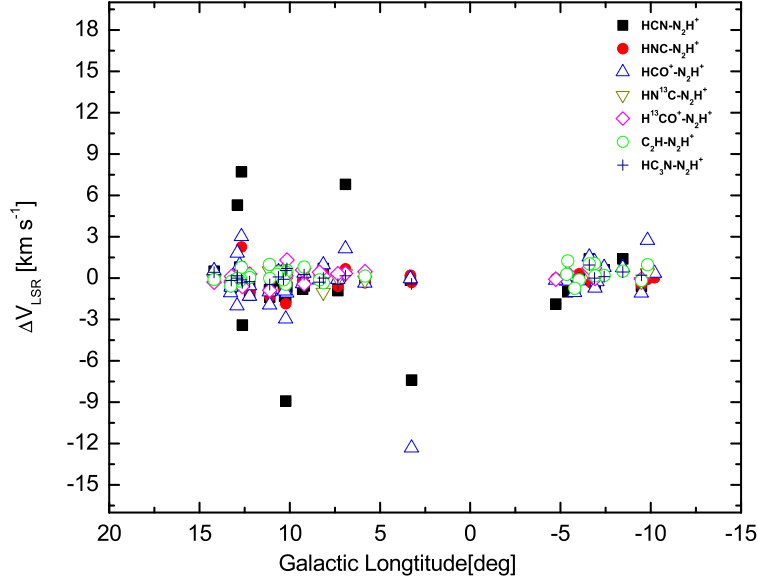


Fig. 8 The centroid velocity differences between $\text{N}_2\text{H}^+(1-0)$ and other lines.

$1_{3/2,2} - 0_{1/2,1}$ and $N_{J,F} = 1_{3/2,1} - 0_{1/2,0}$ are detected in our work (see the spectra in Fig. 7) and their intensity ratio $\frac{C_2H(F=2-1)}{C_2H(F=1-0)}$ is 2.0 (Tucker et al. 1974). But for $\text{N}_2\text{H}^+(1-0)$, we substitute $\int T_{\text{MB}} dv$ for T_{MB} . Because the seven hfss are mixed into three groups with an intensity ratio of 1:5:3 (Yu & Xu 2016), the optical thickness for $\text{N}_2\text{H}^+(1-0)$ can be obtained from the following equation

$$\frac{1 - e^{-r\tau}}{1 - e^{-\tau}} \simeq \frac{\int T_{\text{MB},1} dv}{\int T_{\text{MB},2} dv}. \quad (10)$$

Here $\int T_{\text{MB},1} dv$ is the second component $\text{N}_2\text{H}^+(N_{J,F} = 1_{2,3} - 0_{1,2})$ and $\int T_{\text{MB},2} dv$ is the third component $\text{N}_2\text{H}^+(N_{J,F} = 1_{1,2} - 0_{1,2})$. Therefore, the intensity ratio r here is 5/3. The derived optical depths of $\text{N}_2\text{H}^+(1-0)$ and $\text{C}_2\text{H}(1-0)$ are listed in Columns (4) and (5) of Table 4.

A lot of research suggests $\text{HC}_3\text{N}(10-9)$ is optically thin (e.g. Chen et al. 2013; Yu & Xu 2016). In order to compare our work with other research, such as Vasyunina et al. (2011) and Sanhueza et al. (2012), here we also assume that $\text{HC}_3\text{N}(10-9)$ is optically thin. Then through Equation (8), we get the column densities of $\text{N}_2\text{H}^+(1-0)$, $\text{HN}^{13}\text{C}(1-0)$, $\text{H}^{13}\text{CO}^+(1-0)$, $\text{C}_2\text{H}(1-0)$ and $\text{HC}_3\text{N}(10-9)$. Adopting the abundance ratio of $[^{12}\text{C}]/[^{13}\text{C}] \sim 50$, the column densities of $\text{HNC}(1-0)$ and $\text{HCO}^+(1-0)$ are available. The derived results are shown in Table 4. We also calculate their abundances through the formula $X_{\text{line}} = N_{\text{line}}/N_{\text{H}_2}$.

Table 5 includes the calculated results. From Tables 4 and 5, we find that the median column densities of $\text{N}_2\text{H}^+(1-0)$, $\text{HNC}(1-0)$, $\text{HCO}^+(1-0)$, $\text{C}_2\text{H}(1-0)$ and $\text{HC}_3\text{N}(10-9)$ are $(4.05 \pm 0.18) \times 10^{13}$, $(1.40 \pm 0.28) \times 10^{14}$, $(0.89 \pm 0.20) \times 10^{14}$, $(4.90 \pm 0.74) \times 10^{14}$ and $(1.22 \pm 0.12) \times 10^{13} \text{ cm}^{-2}$ corresponding to the median abundances of $(1.42 \pm 0.13) \times 10^{-9}$, $(0.28 \pm 0.07) \times 10^{-8}$, $(0.25 \pm 0.05) \times 10^{-8}$, $(1.85 \pm 0.26) \times 10^{-8}$ and $(2.58 \pm 0.50) \times 10^{-10}$ in HII/PDR regions, and $(2.92 \pm 0.16) \times 10^{13}$, $(1.2 \pm 0.2) \times 10^{14}$, $(0.69 \pm 0.16) \times 10^{14}$, $(3.67 \pm 0.58) \times 10^{14}$ and $(1.28 \pm 0.17) \times 10^{13} \text{ cm}^{-2}$ corresponding to the median abundances of $(1.21 \pm 0.13) \times 10^{-9}$, $(0.34 \pm 0.08) \times 10^{-8}$, $(0.17 \pm 0.07) \times 10^{-8}$, $(1.10 \pm 0.22) \times 10^{-8}$ and $(3.86 \pm 0.58) \times 10^{-10}$ in the proto-stellar clumps respectively. Compared with previous studies (Vasyunina et al. 2011; Sanhueza et al. 2012; Yu & Xu 2016), the column densities of the five species are at the same magnitude as them, but the abundances of the species are at a magnitude lower than those of Vasyunina et al. (2011) and Sanhueza et al. (2012) while being consistent with those of Yu & Xu (2016). This implies that the BGPS clumps are less dense than the infrared dark clouds (IRDCs) but similar to the sources from the Midcourse Space Experiment. In addition, we show the histograms of $\text{N}_2\text{H}^+(1-0)$, $\text{HNC}(1-0)$, $\text{HCO}^+(1-0)$, $\text{C}_2\text{H}(1-0)$ and $\text{HC}_3\text{N}(10-9)$ abundances in proto-stellar and HII/PDR stages in Figure 9. From Figure 9, we find that the abundances of nitrogen-bearing

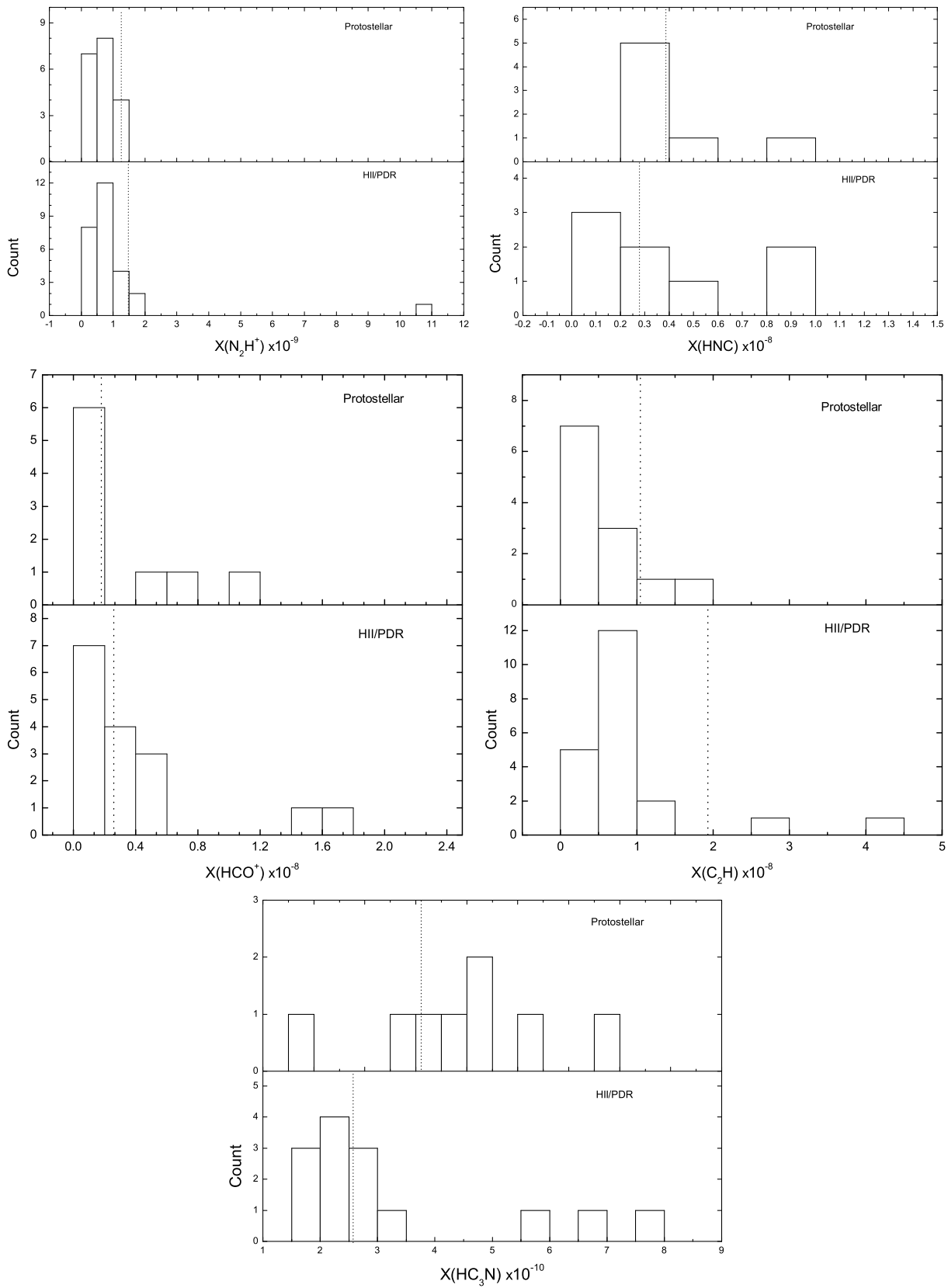


Fig. 9 Abundance histograms of N_2H^+ , HNC, HCO^+ , C_2H and HC_3N in protostellar clumps (top subpanels) and HII/PDR regions (bottom subpanels). The dashed vertical lines indicate their median values.

molecules seem to decrease with evolution, while those of oxygen-bearing molecules and C_2H increase.

4 DISCUSSION

4.1 Non-thermal Velocity

Since $N_2H^+(1-0)$ is optically thin and detected in all the clumps, this molecule can cast light upon the internal properties of clumps. The line width of $N_2H^+(1-0)$ responds to the internal motions within clumps, such as thermal motions, turbulence, inflows and outflows.

In Table 3, G003.254+00.410, which has the highest velocity dispersion of 11.1 km s^{-1} , will not be discussed in this subsection because of the complexity near the Galactic center. The velocity dispersions of our sample are in the range of $1.27-6.27 \text{ km s}^{-1}$, with up to 82% of clumps having $\sigma_{\text{obs}} \geq 2.0 \text{ km s}^{-1}$. In contrast to previous studies (Anglada et al. 1996; Dunham et al. 2011) with a range of $1-4 \text{ km s}^{-1}$ and 98% of their sources less than $\leq 2 \text{ km s}^{-1}$, most of our sources are more active internally.

The observed line width is attributed to thermal and non-thermal motions of the gas. We can determine the non-thermal velocity dispersion by removing the thermal contribution to the observed line width through the following expression

$$\sigma_{\text{NT}} = \sqrt{\frac{\sigma_{\text{obs}}^2}{8 \ln 2} - \frac{kT_{\text{kin}}}{29m_{\text{H}}}}, \quad (11)$$

in which σ_{obs} is the observed $N_2H^+(1-0)$ FWHM (in Table 3). k is the Boltzmann constant and T_{kin} is the kinetic temperature of the gas (here approximated as the dust temperature). Here $\frac{kT_{\text{kin}}}{29m_{\text{H}}}$ is thermal broadening. The median values of σ_{NT} in proto-stellar clumps and HII/PDR regions are 1.17 ± 0.17 and $1.29 \pm 0.13 \text{ km s}^{-1}$, respectively. Moreover, we plot the relations between σ_{NT} and T_{kin} as well as the integrated 1.1 mm flux density ($S_{1.1}$) in Figure 10. The blue open circles represent proto-stellar clumps and the black squares are HII/PDR regions. The black curve in the left panel marks the thermal sound speed as $a = (kT_{\text{kin}}/\mu m_{\text{H}})^{1/2}$, which is at least three times smaller than the corresponding non-thermal line width. It indicates that non-thermal motions dominate the line broadening of N_2H^+ in these clumps. The low correlation coefficients around 0.3 of σ_{NT} with T_{kin} and $S_{1.1}$ suggest that both the temperature and the 1.1 mm flux density seem to influence the non-thermal motions to some extent. Furthermore, σ_{NT} as a whole

probably increases with T_{kin} as well as $\log(S_{1.1})$ in each stage.

4.2 The Mass-size Relationships

Figure 11 presents the relationships between mass and size for both proto-stellar and HII/PDR stages. The black shadowed region there represents a parameter space devoid of massive star formation, determined by Kauffmann & Pillai (2010). The yellow filled area indicates the region of massive pro-cluster candidates (e.g. Bressert et al. 2012). The red horizontal dashed line marks $M = 10^3 M_{\odot}$. The solid blue and black lines indicate the respective least squares bisector fittings to them expressed as empirical relations of $\log(M/M_{\odot})_{\text{protostellar}} = (2.02 \pm 0.10) \log(R \text{ pc}^{-1}) + (2.78 \pm 0.05)$ with a correlation coefficient of 0.97, and $\log(M/M_{\odot})_{\text{HII/PDR}} = (2.00 \pm 0.12) \log(R \text{ pc}^{-1}) + (2.80 \pm 0.06)$ with a correlation coefficient of 0.90. The mass and radius show a close positive correlation and a power-law relationship with each other. When $M \geq 10^3 M_{\odot}$, the clumps have a high potential to form high-mass stars, otherwise, the chance of a clump forming a massive star is merely up to 28%. As a whole, based on Figure 11, about 74.1% of HII/PDR regions and 78.9% of proto-stellar clumps have an opportunity to form high-mass stars. Moreover, the slope of the mass-radius relation in our work seems to be a constant around 2.00, which is similar to that of He et al. (2016) considering the uncertainty. However, more explorations are required to justify this conclusion.

4.3 Virial Mass

Based on the analysis of He et al. (2016), we can assess the virial mass of each clump by utilizing the line width of $N_2H^+(1-0)$ (Urquhart et al. 2013)

$$\frac{M_{\text{vir}}}{M_{\odot}} = \frac{783}{7 \ln 2} \left(\frac{R}{\text{pc}} \right) \left(\frac{\sigma_{\text{avg}}}{\text{km s}^{-1}} \right)^2, \quad (12)$$

where R is the effective radius that is derived from Equation (6), which is used in Table 1, and σ_{avg} is the average velocity dispersion of gas via

$$\sigma_{\text{avg}} = (\sigma_{\text{obs}})^2 + 8 \ln 2 \times \frac{kT_{\text{kin}}}{m_{\text{H}}} \left(\frac{1}{\mu_p} - \frac{1}{\mu_{N_2H^+}} \right), \quad (13)$$

where $\mu_p \simeq 2.33$ and $\mu_{N_2H^+} = 29$ are the mean molecular masses of molecular hydrogen and N_2H^+ , respectively. Since $N_2H^+(1-0)$ lines are optically thin in all the

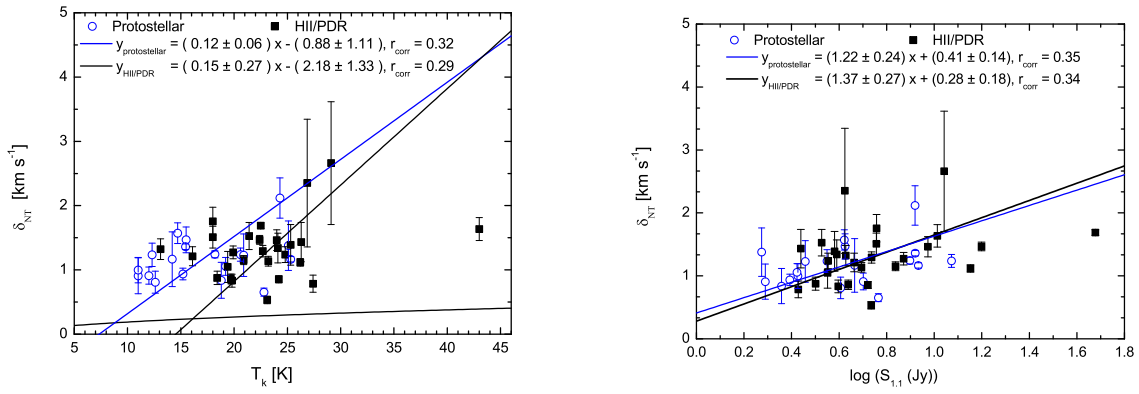


Fig. 10 Left panel: non-thermal velocity dispersion of N_2H^+ vs. the kinetic temperature. The *black squares* are for HII/PDR regions and the *blue open circles* represent proto-stellar clumps. The *black curve* indicates the thermal sound speed given by $a = (kT_{\text{kin}}/\mu m_{\text{H}})^{1/2}$. Right panel: non-thermal velocity dispersion of N_2H^+ vs. the integrated 1.1 mm flux density. The *black* and *blue* solid lines are the least squares bisector fittings toward the HII/PDR regions and the proto-stellar clumps, respectively.

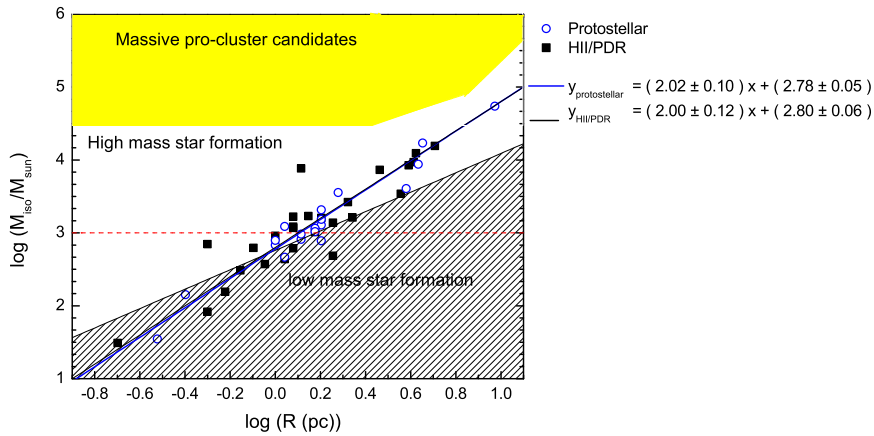


Fig. 11 The mass-size relationships of HII/PDR regions (*black squares*) and the proto-stellar clumps (*blue open circles*) with mass determined. The *black shaded region* represents the parameter space that is devoid of massive star formation, where $\log(M/M_{\odot}) = 1.33 \log(R \text{ pc}^{-1}) + 2.76$ (Kauffmann & Pillai 2010). The *yellow shadowed area* indicates the region in which young massive cluster progenitors are expected to found (Bressert et al. 2012, e.g.). The *solid black* and *blue* lines show the least squares bisector fittings to HII/PDR regions and proto-stellar clumps, respectively. The *red dashed horizon line* represents $M = 1000 M_{\odot}$.

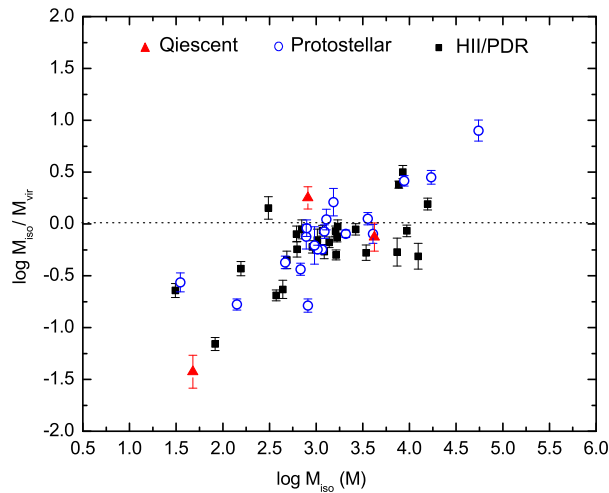


Fig. 12 Virial ratio $\log(M_{\text{iso}}/M_{\text{vir}})$ as a function of $\log(M_{\text{iso}}/M_{\odot})$ for HII/PDR regions (*black squares*), proto-stellar clumps (*blue open circles*) and pre-stellar clumps (*red triangles*). The *black horizontal line* indicates the locus of gravitational equilibrium for thermal and kinematic energies.

clumps (see the τ values of $\text{N}_2\text{H}^+(1-0)$ in Table 4) and the spectra are extracted from the peak positions, σ_{avg} are overestimated which results in the overestimated M_{vir} . The virial masses of 50 sources are presented in Table 1. The uncertainties in the parentheses come from measurement errors of the line widths.

We plot the virial ratios $\log(M_{\text{iso}}/M_{\text{vir}})$ versus the clump masses in the stages from pre-stellar to proto-stellar to HII/PDR in Figure 12. The dashed horizontal line marks the line of gravitational stability. Sources with ratios $\log(M_{\text{iso}}/M_{\text{vir}})$ over this line are gravitationally bound and then collapse to possibly form stars, otherwise the clumps may be gravitationally unbound.

In Figure 12, we find that over 65% of sources in various evolutionary stages are gravitationally unbound and have no opportunity to form stars at present, which is paradoxical with regard to the indicators of star formation, such as SiO (2–1) emission, infall motions (discussed in Sect. 4.5) and 24 μm sources. The likely explanation is that most of the clumps contain a set of sub-cores rather than only one core and hence most of the clumps' envelopes are gravitationally unbound.

4.4 Chemical Correlations between Different Species

The ratio of $\text{N}_2\text{H}^+/\text{HCO}^+$ emission can be a chemical indicator of the evolution of the clump, since N_2H^+ and HCO^+ have opposite chemical behavior with respect to CO. HCO^+ can be produced by two chemical reactions of $\text{H}_3^+ + \text{CO} \rightarrow \text{HCO}^+ + \text{H}_2$ and $\text{N}_2\text{H}^+ + \text{CO} \rightarrow \text{HCO}^+ + \text{N}_2$ (Jørgensen et al. 2004; Schlingman et al. 2011). As CO is frozen onto dust grains at high densities ($n > 10^4 \text{ cm}^{-3}$) and low temperatures ($T_{\text{kin}} < 20 \text{ K}$), the large ratio of $\text{N}_2\text{H}^+/\text{HCO}^+$ emission indicates a cold and dense environment. Otherwise, with temperature rising, CO is eventually freed from the dust grains, which then results in the destruction of N_2H^+ and production of HCO^+ . Consequently, the integrated intensity ratio of $\text{N}_2\text{H}^+/\text{HCO}^+$ should decrease with temperature. Moreover, N_2H^+ does not start to be depleted on dust grains until densities reach 10^6 cm^{-3} (Tafalla et al. 2004; Flower et al. 2006), which can be excluded in our work (see Table 1).

Figure 13 shows the variation of integrated intensity ratio $\text{N}_2\text{H}^+(1-0)$ to $\text{HCO}^+(1-0)$ versus the dust temperature and integrated flux at 1.1 mm towards two evolutionary stages (proto-stellar and HII/PDR). The integrated intensity ratios $I(\text{N}_2\text{H}^+/\text{HCO}^+)$ actually decline

as power-law functions and have negative correlations ($r_{\text{corr-protostellar}} = -0.21$ and $r_{\text{corr-HII/PDR}} = -0.40$) with T_{dust} in both stages, especially in the later evolutionary stage. However, the relations between the ratio of $\text{N}_2\text{H}^+/\text{HCO}^+$ emission and the integrated flux are positive in these two stages despite the lower correlation coefficients ($r_{\text{corr(protostellar)}} = 0.07$ and $r_{\text{corr(HII/PDR)}} = 0.15$), which means there are almost no correlations. Even so, we still apply least squares bisector fittings between $\log I(\text{N}_2\text{H}^+/\text{HCO}^+)$ and $\log(S_{1.1})$ (see the top-right panel in Fig. 13) and find two similar linear functions with both slopes being 1.0. The poor correlations further suggest that the BGPS clumps are unlikely to be single massive cores but probably consist of multiple smaller cores, between which the fraction of cold, dense and CO-depleted gas is different (Shirley et al. 2013). Comparing these two subfigures in Figure 13 (slopes and correlation coefficients), we can find that if the density is less than 10^6 cm^{-3} , temperature plays a more vital role in the chemical evolution of molecules.

Furthermore, we also present the abundance relations between four species (N_2H^+ , HCO^+ , C_2H and HC_3N) in Figure 13 and find that the abundances of nitrogen-bearing molecules (N_2H^+ and HC_3N) dramatically decrease compared to those of the oxygen-bearing molecule (HCO^+) in both proto-stellar and HII/PDR clumps. This probably suggests that HCO^+ is produced by the destruction of the nitrogen-bearing molecules and N_2H^+ is the primary contribution, since the abundance of HC_3N seems not to vary in the HCO^+ relatively more abundant region. On the other hand, the abundance of C_2H appears to fluctuate with HCO^+ . It might be related to the major destruction route in which C_2H reacts with O to form CO (Pan et al. 2017). C_2H seems to have nothing to do with N_2H^+ according to their abundance relationship in Figure 13. Combined with Table 5, the nitrogen-bearing molecules are likely to be more abundant in the earlier stages while the oxygen-bearing species and C_2H are sparse. Furthermore, C_2H is the most abundant species, followed by the sequence HCO^+ , N_2H^+ , HNC and HC_3N .

4.5 Infall Candidates

Based on two methods to identify the infall candidates (e.g. Mardones et al. 1997; Fuller et al. 2005; Wu et al. 2005; Sun & Gao 2009; Chen et al. 2013; Liu et al. 2014), we find three new infall candidates G010.214–

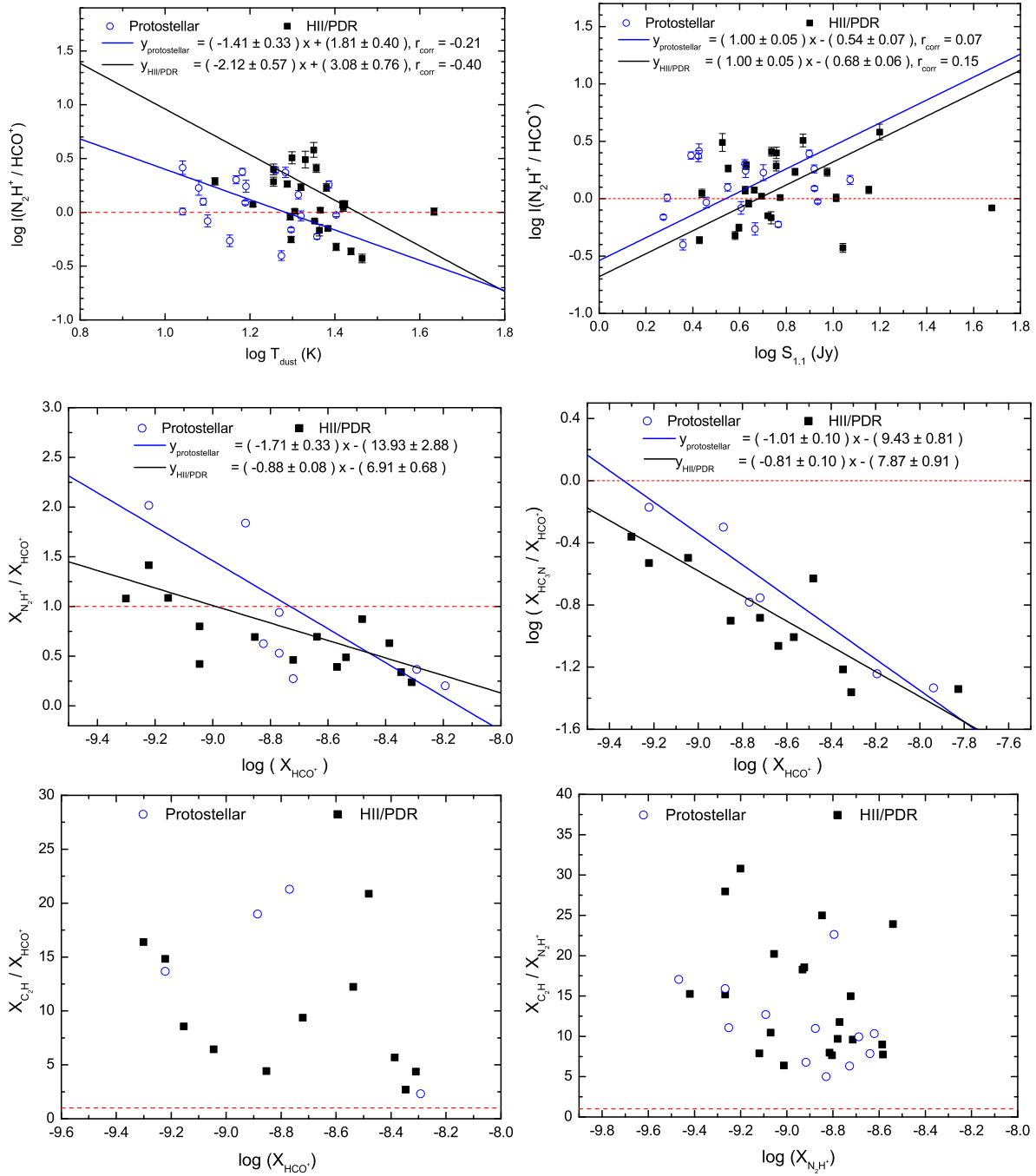


Fig. 13 *Top-left*: plot of integrated intensity ratio $\log(N_2H^+/HCO^+)$ vs. the dust temperature $\log T_{\text{dust}} \text{ (K)}$. *Top-right*: plot of integrated intensity ratio $\log(N_2H^+/HCO^+)$ vs. the integrated 1.1 mm flux $\log S_{1.1} \text{ (Jy)}$. *Middle-left*: plot of abundance ratio $X_{N_2H^+}/X_{HCO^+}$ vs. $\log(X_{HCO^+})$. The black and blue lines are the linear fittings for the clumps in two different evolutionary stages (HII/PDR and proto-stellar). *Middle-right*: plot of abundance ratio $\log(X_{HC_3N}/X_{HCO^+})$ vs. $\log(X_{HCO^+})$. The black and the blue curves indicate the power fittings at two different evolutionary stages-HII/PDR (black squares) and proto-stellar (blue open circles). *Bottom-left*: plot of abundance ratio X_{C_2H}/X_{HCO^+} vs. $\log(X_{HCO^+})$ in proto-stellar clumps (blue open circles) and HII/PDR regions (black squares). *Bottom-right*: plot of abundance ratio $X_{C_2H}/X_{N_2H^+}$ vs. $\log(X_{N_2H^+})$ in proto-stellar clumps (blue open circles) and HII/PDR regions (black squares). The red dashed lines in the subfigures represent $y = 1$.

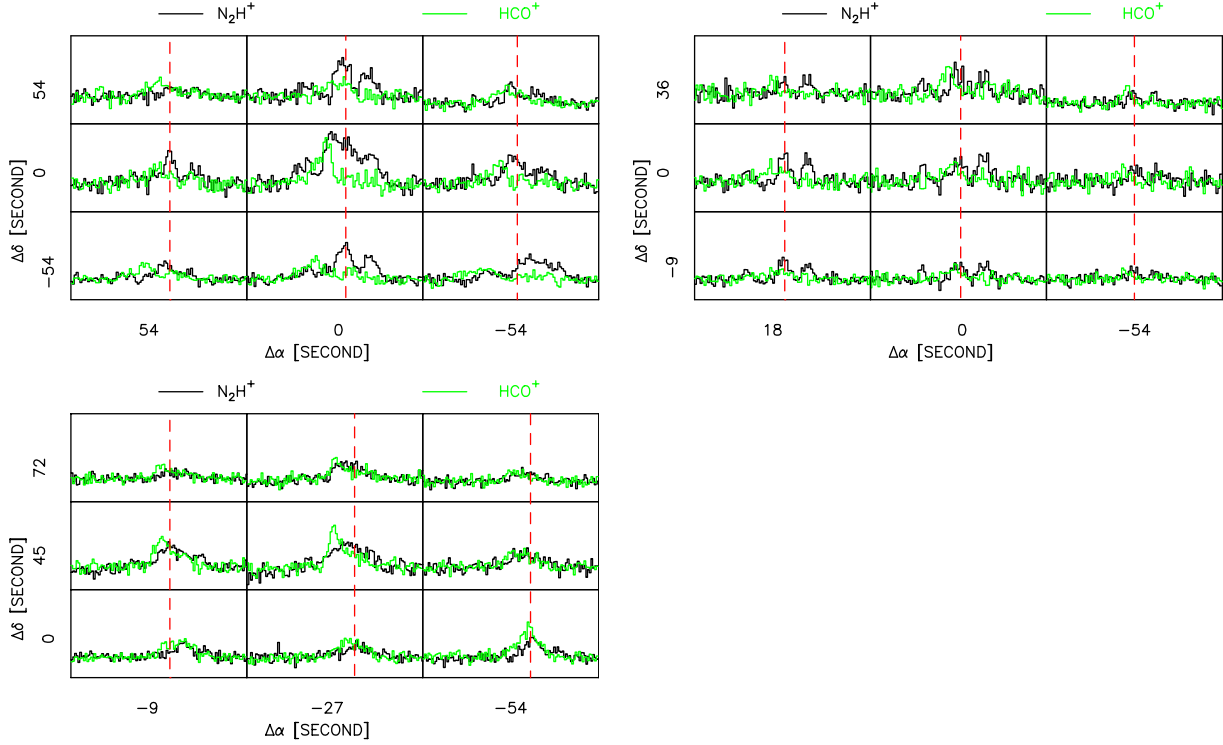


Fig. 14 The mapping grids for the three infall candidates G010.214–00.324 (*top-left*), G011.121–00.128 (*top-right*) and G012.215–00.118(a) (*bottom-left*). The *black lines* are for N_2H^+ and the *green lines* represent HCO^+ . The grids also display scales where the infall motions exist.

00.324, G011.121–00.128 and G012.215–00.118(a). In a quantifiable way, δV is defined as $\delta V = (V_{\text{thick}} - V_{\text{thin}}) / \Delta V_{\text{thin}}$ and is the asymmetry parameter to judge the infall motions with $\delta V > 0.25$ for red asymmetry and $\delta V < -0.25$ for blue asymmetry. Here V_{thick} represents the line peak velocity of the optically thick line and V_{thin} , an optically thin tracer, measures the systemic velocity. ΔV_{thin} is the line width of the optically thin line. In our work, N_2H^+ represents the optically thin case while HCO^+ and HNC are optically thick.

The asymmetry parameters δV of HCO^+ and HNC for the three newly discovered infall candidates are listed in Table 6 according to the observed parameters in Table 3. Both G010.214–00.324 and G011.121–00.128 exhibit a blue asymmetry in HCO^+ and HNC lines, while G012.215–00.118(a) shows a blue asymmetry in the HCO^+ line but not asymmetry in the HNC line. Following the criterion utilized in He et al. (2015), infall candidates must have a blue skewed profile in at least one optically thick line ($HCO^+(1-0)$ or $HNC(1-0)$), no red skewed profile in the other optically thick line and no spatial difference in the mapping observation. These three clumps are likely to be infall candidates.

In order to ensure that the infall motions really exist on large scales, we make mapping grids for the three infall candidates in Figure 14. Each mapping shows the whole region where the blue skewed profiles occur, and hence can be used to compute a measure of the infall motion.

From Figure 14, we can obtain that the infall motion sizes for G010.214–00.324, G011.121–00.128 and G012.215–00.118(a) are $1.64 \text{ pc} \times 1.64 \text{ pc}$ ($1.8' \times 1.8'$), $1.06 \text{ pc} \times 0.66 \text{ pc}$ ($1.2' \times 0.75'$) and $3.05 \text{ pc} \times 4.88 \text{ pc}$ ($0.75' \times 1.2'$) respectively. Therefore, these three clumps actually show large-scale infall motions. Furthermore, we roughly estimate their infall rate by the following formula (López-Sepulcre et al. 2010)

$$\begin{aligned} \dot{M}_{\text{inf}} &= 4\pi\mu_{H_2}m_H r^2 V_{\text{inf}} n \\ &= 3.15 \times 10^{-4} \left(\frac{r}{\text{pc}}\right)^2 \left(\frac{V_{\text{inf}}}{\text{km s}^{-1}}\right) \left(\frac{n}{\text{cm}^{-3}}\right), \end{aligned} \quad (14)$$

where $V_{\text{inf}} = V_{N_2H^+} - V_{HCO^+}$ is a rough estimate of the infall velocity, $r = \sqrt{r_{\text{maj}} r_{\text{min}}}$ is the equivalent radius of the infall region and n is the volume density described in Section 3.2. Through Equation (14), we get the infall rates for G010.214–00.324, G011.121–

Table 6 Profiles of the Possible Infall Candidates

Clump name ^a	δV	δV	Profile
	HCO ⁺ (1–0)	HNC(1–0)	
(1)	(2)	(3)	(4)
*G010.214–00.324	–0.59(0.06)	–0.37(0.05)	B,B
*G011.121–00.128	–1.17(0.18)	–0.43(0.09)	B,B
*G012.215–00.118(a)	–0.25(0.09)	–0.19(0.08)	B,N

Notes: ^a Sources are named by Galactic coordinates of BGPS sources: An * indicates infall candidates. The HCO⁺(1–0) and HNC(1–0) profiles are evaluated as follows: B denotes a blue profile, R denotes a red profile and N denotes neither blue nor red. Quantities in parentheses give the uncertainties in units of 0.01. The columns are as follows: (1) clump name; (2) asymmetry of HCO⁺(1–0); (3) asymmetry of HNC(1–0); (4) profile of HCO⁺(1–0) and HNC(1–0).

00.128 and G012.215–00.118(a) to be $(3.4 \pm 0.4) \times 10^{-3}$, $(1.6 \pm 0.2) \times 10^{-3}$ and $(6.5 \pm 2.5) \times 10^{-3} M_{\odot} \text{ yr}^{-1}$ respectively, which have a similar magnitude as previous studies (López-Sepulcre et al. 2010; He et al. 2016).

5 SUMMARY

We perform an investigation of 48 high-mass clumps selected on the basis of the BGPS and MALT90 survey data and aim at studying the fragmentation, classification, physical and chemical features, chemical evolution of dense gases and star formation activities. Our main results are summarized as follows:

- (1) Combining the 1.1 mm continuum data with molecular emission, we find that only two clumps (G012.215–00.118 and G354.000+00.474) of our sample show sub-structures and all the remaining clumps have a single-core structure. This might be attributed to similar spatial resolutions between the BGPS continuum data (33'') and the MALT90 survey (36''). Among the final 50 clumps, 27 are HII/PDR, 19 are pro-stellar, 3 are pre-stellar while 1 is uncertain. These clumps are concentrated on the molecular ring and the expanding arm.
- (2) Eleven species are detected in our work. They are N₂H⁺(1–0), HNC(1–0), HCO⁺(1–0), HCN(1–0), HN¹³C(1–0), H¹³CO⁺(1–0), C₂H(1–0), HC₃N(10–9), SiO(2–1), HNC(4_{4,0} – 3_{0,3}) and ¹³CS(2–1). Among them, N₂H⁺(1–0) and HNC(1–0) are detected in all the fields. The detection rates of other N-bearing molecular lines decline with evolution except for HC₃N(10–9), while those of O-bearing spectra show an inverse relation. The reason why the detection rate of HC₃N(10–9) rises with evolution may be that this molecule is related to the C-

chain generation and is an indicator of hot cores. A comparison of centroid line velocities for each clump indicates that nine molecular lines can provide accurate systemic velocities for a clump except for HCO⁺ and HCN, whose V_{LSR} can deviate up to 12 km s^{–1} from those of other molecular transition lines.

- (3) The temperature, mass and volume density increase as the clumps evolve, while the H₂ column density first shows an increase from pre-stellar to proto-stellar then almost remains steady at the HII/PDR stage. However, the clumps on the whole accumulate material efficiently as they evolve. Both mass distributions of the clumps at proto-stellar and HII/PDR are concentrated around a median value of 1000 M_{\odot} .
- (4) The masses and sizes of clumps in both the proto-stellar and HII/PDR stages show close correlations with each other and obey two power-law functions with indexes of 2.02 ± 0.10 and 2.00 ± 0.12 , respectively, which are sharper than those of Kauffmann & Pillai (2010) (1.33). The similar indexes in two stages may suggest that the mass-size relationship does not vary with evolution. More research should be done to justify this conclusion. Also, more than 70% of clumps at these two stages should be capable of forming high-mass stars, but the envelopes of most clumps are gravitationally unbound at the moment, indicating most of our clumps probably consist of several inner cores rather than a single structure.
- (5) The abundance ratios of N-bearing species to O-bearing species decrease sharply as the clumps evolve, indicating the trend of destruction of N-bearing species and production of O-bearing species

in the later evolutionary phase. Therefore, the ratios of N-bearing species to O-bearing molecules can be the chemical indicators of evolution. In addition, C₂H is the most abundant molecule in all the stages and its chemical evolution may pose a slight impact on that of HCO⁺.

- (6) Three infall candidates are identified. They are G010.214–00.324, G011.121–00.128 and G012.215–00.118(a), which all exhibit large-scale infall motions with infall rates of $(3.4 \pm 0.4) \times 10^{-3}$, $(1.6 \pm 0.2) \times 10^{-3}$ and $(6.5 \pm 2.5) \times 10^{-3} M_{\odot} \text{ yr}^{-1}$ respectively.

Acknowledgements We are very grateful to the anonymous referee for his/her helpful comments and suggestions. This research has made use of data products from the *Millimetre Astronomy Legacy Team 90 GHz (MALT90)* survey, and also used NASA/IPAC Infrared Science Archive, which is operated by the Jet Propulsion Laboratory, California Institute of Technology, under contract with the National Aeronautics and Space Administration. This work is supported by the National Natural Science Foundation of China (Nos. 11363004 and 11403042). This work is also supported by the National Key Basic Research Program of China (No. 2015CB857100).

References

- Aguirre, J. E., Ginsburg, A. G., Dunham, M. K., et al. 2011, *ApJS*, 192, 4
- Anglada, G., Estalella, R., Pastor, J., Rodriguez, L. F., & Haschick, A. D. 1996, *ApJ*, 463, 205
- Battersby, C., Bally, J., Ginsburg, A., et al. 2011, *A&A*, 535, A128
- Beuther, H., Churchwell, E. B., McKee, C. F., & Tan, J. C. 2007, *Protostars and Planets V*, 165
- Bonnell, I. A., Bate, M. R., Clarke, C. J., & Pringle, J. E. 2001, *MNRAS*, 323, 785
- Bonnell, I. A., Vine, S. G., & Bate, M. R. 2004, *MNRAS*, 349, 735
- Bonnell, I. A., & Bate, M. R. 2006, *MNRAS*, 370, 488
- Bressert, E., Ginsburg, A., Bally, J., et al. 2012, *ApJ*, 758, L28
- Chen, X., Gan, C.-G., Ellingsen, S. P., et al. 2013, *ApJS*, 206, 22
- Cyganowski, C. J., Whitney, B. A., Holden, E., et al. 2008, *AJ*, 136, 2391
- Dunham, M. K., Rosolowsky, E., Evans, II, N. J., Cyganowski, C., & Urquhart, J. S. 2011, *ApJ*, 741, 110
- Faimali, A., Thompson, M. A., Hindson, L., et al. 2012, *MNRAS*, 426, 402
- Flower, D. R., Pineau Des Forêts, G., & Walmsley, C. M. 2006, *A&A*, 456, 215
- Fuller, G. A., Williams, S. J., & Sridharan, T. K. 2005, *A&A*, 442, 949
- Glenn, J., Ade, P. A. R., Amarie, M., et al. 2003, in *Proc. SPIE*, 4855, Millimeter and Submillimeter Detectors for Astronomy, eds. T. G. Phillips & J. Zmuidzinas, 30
- Glenn, J., Aguirre, J., Bally, J., et al. 2009, in *ASPC Series*, 417, Submillimeter Astrophysics and Technology: a Symposium Honoring Thomas G. Phillips, eds. D. C. Lis, J. E. Vaillancourt, P. F. Goldsmith, T. A. Bell, N. Z. Scoville, & J. Zmuidzinas, 277
- Griffin, M. J., Abergel, A., Abreu, A., et al. 2010, *A&A*, 518, L3
- Guzmán, A. E., Sanhueza, P., Contreras, Y., et al. 2015, *ApJ*, 815, 130
- Haig, D. J., Ade, P. A. R., Aguirre, J. E., et al. 2004, in *Proc. SPIE*, 5498, Z-Spec: a Broadband Millimeter-wave Grating Spectrometer: Design, Construction, and First Cryogenic Measurements, eds. C. M. Bradford, P. A. R. Ade, J. E. Aguirre, J. J. Bock, M. Dragovan, L. Duband, L. Earle, J. Glenn, H. Matsuhara, B. J. Naylor, H. T. Nguyen, M. Yun, & J. Zmuidzinas, 78
- He, Y.-X., Zhou, J.-J., Esimbek, J., et al. 2015, *MNRAS*, 450, 1926
- He, Y.-X., Zhou, J.-J., Esimbek, J., et al. 2016, *MNRAS*, 461, 2288
- Hoq, S., Jackson, J. M., Foster, J. B., et al. 2013, *ApJ*, 777, 157
- Jackson, J. M., Rathborne, J. M., Foster, J. B., et al. 2013, *PASA*, 30, e057
- Jørgensen, J. K., Schöier, F. L., & van Dishoeck, E. F. 2004, *A&A*, 416, 603
- Kauffmann, J., Bertoldi, F., Bourke, T. L., Evans, II, N. J., & Lee, C. W. 2008, *A&A*, 487, 993
- Kauffmann, J., & Pillai, T. 2010, *ApJ*, 723, L7
- Keto, E., & Rybicki, G. 2010, *ApJ*, 716, 1315
- Ladd, N., Purcell, C., Wong, T., & Robertson, S. 2005, *PASA*, 22, 62
- Liu, X.-L., Wang, J.-J., & Xu, J.-L. 2014, *MNRAS*, 443, 2264
- López-Sepulcre, A., Cesaroni, R., & Walmsley, C. M. 2010, *A&A*, 517, A66
- Mardones, D., Myers, P. C., Tafalla, M., et al. 1997, *ApJ*, 489, 719
- McKee, C. F., & Tan, J. C. 2002, *Nature*, 416, 59
- McKee, C. F., & Tan, J. C. 2003, *ApJ*, 585, 850
- Motte, F., Andre, P., & Neri, R. 1998, *A&A*, 336, 150
- Müller, H. S. P., Schlöder, F., Stutzki, J., & Winnewisser, G. 2005, *Journal of Molecular Structure*, 742, 215
- Müller, H. S. P., Thorwirth, S., Roth, D. A., & Winnewisser,

- G. 2001, *A&A*, 370, L49
- Ossenkopf, V., & Henning, T. 1994, *A&A*, 291, 943
- Padovani, M., Walmsley, C. M., Tafalla, M., Galli, D., & Müller, H. S. P. 2009, *A&A*, 505, 1199
- Pagani, L., Daniel, F., & Dubernet, M.-L. 2009, *A&A*, 494, 719
- Pan, Z., Li, D., Chang, Q., et al. 2017, *ApJ*, 836, 194
- Paron, S., Weidmann, W., Ortega, M. E., Albacete Colombo, J. F., & Pichel, A. 2013, *MNRAS*, 433, 1619
- Poglitsch, A., Waelkens, C., Geis, N., et al. 2010, *A&A*, 518, L2
- Purcell, C. R., Balasubramanyam, R., Burton, M. G., et al. 2006, *MNRAS*, 367, 553
- Reid, M. J., Dame, T. M., Menten, K. M., & Brunthaler, A. 2016, *ApJ*, 823, 77
- Reitblat, A. A. 1980, *Soviet Astronomy Letters*, 6, 406
- Rosolowsky, E., Dunham, M. K., Ginsburg, A., et al. 2010, *ApJS*, 188, 123
- Sanhueza, P., Jackson, J. M., Foster, J. B., et al. 2012, *ApJ*, 756, 60
- Schlingman, W. M., Shirley, Y. L., Schenk, D. E., et al. 2011, *ApJS*, 195, 14
- Shirley, Y. L., Ellsworth-Bowers, T. P., Svoboda, B., et al. 2013, *ApJS*, 209, 2
- Shu, F. H., Adams, F. C., & Lizano, S. 1987, *ARA&A*, 25, 23
- Spielfiedel, A., Feautrier, N., Najar, F., et al. 2012, *MNRAS*, 421, 1891
- Sun, Y., & Gao, Y. 2009, *MNRAS*, 392, 170
- Tafalla, M., Myers, P. C., Caselli, P., & Walmsley, C. M. 2004, *A&A*, 416, 191
- Tan, J. C., Beltrán, M. T., Caselli, P., et al. 2014, *Protostars and Planets VI*, 149
- Traficante, A., Calzoletti, L., Veneziani, M., et al. 2011, *MNRAS*, 416, 2932
- Tucker, K. D., Kutner, M. L., & Thaddeus, P. 1974, *ApJ*, 193, L115
- Urquhart, J. S., Moore, T. J. T., Schuller, F., et al. 2013, *MNRAS*, 431, 1752
- Vasyunina, T., Linz, H., Henning, T., et al. 2011, *A&A*, 527, A88
- Wang, K., Testi, L., Ginsburg, A., et al. 2015, *MNRAS*, 450, 4043
- Watson, C., Povich, M. S., Churchwell, E. B., et al. 2008, *ApJ*, 681, 1341
- Wu, Y., Zhu, M., Wei, Y., et al. 2005, *ApJ*, 628, L57
- Yu, N., & Xu, J. 2016, *ApJ*, 833, 248
- Zhang, C.-P., Li, G.-X., Wyrowski, F., et al. 2016, *A&A*, 585, A117
- Zinnecker, H., & Yorke, H. W. 2007, *ARA&A*, 45, 481